Bright galaxy sample in the Kilo-Degree Survey Data Release 4:

Bright galaxy sample in the Kilo-Degree Survey Data Release 4

Selection, photometric redshifts, and physical properties

M. Bilicki[1]⋆, A. Dvornik[2, 3]⋆⋆, H. Hoekstra[3]⋆⋆⋆, A.H. Wright[2], N.E. Chisari[4], M. Vakili[3],
M. Asgari[5], B. Giblin[5], C. Heymans[5, 2], H. Hildebrandt[2], B.W. Holwerda[6], A. Hopkins[7], H. Johnston[4], A. Kannawadi[8],
K. Kuijken[3], S.J. Nakoneczny[9], H.Y. Shan[10, 11], A. Sonnenfeld[3], and E. Valentijn[12]

1 Center for Theoretical Physics, Polish Academy of Sciences, al. Lotników 32/46, 02-668 Warsaw, Poland
2 Ruhr University Bochum, Faculty of Physics and Astronomy, Astronomical Institute (AIRUB), German Centre for Cosmological Lensing, 44780 Bochum, Germany
3 Leiden Observatory, Leiden University, P.O. Box 9513, NL-2300 RA Leiden, The Netherlands
4 Institute for Theoretical Physics, Utrecht University, Princetonplein 5, 3584 CC Utrecht, The Netherlands
5 Institute for Astronomy, University of Edinburgh, Blackford Hill, Edinburgh, EH9 3HJ, UK
6 Department of Physics and Astronomy, University of Louisville, 102 Natural Science Building, Louisville KY 40292, USA
7 Australian Astronomical Optics, Macquarie University, 105 Delhi Rd, North Ryde, NSW 2113, Australia
8 Department of Astrophysical Sciences, Princeton University, 4 Ivy Lane, Princeton, NJ 08544, USA
9 National Centre for Nuclear Research, Astrophysics Division, ul. Pasteura 7, 02-093 Warsaw, Poland
10 Shanghai Astronomical Observatory (SHAO), Nandan Road 80, Shanghai 200030, China
11 University of Chinese Academy of Sciences, Beijing 100049, China
12 Kapteyn Institute, University of Groningen, PO Box 800, NL 9700 AV Groningen, The Netherlands

ABSTRACT

We present a bright galaxy sample with accurate and precise photometric redshifts (photo-zs), selected using $ugriZYJHK_s$ photometry from the Kilo-Degree Survey (KiDS) Data Release 4 (DR4). The highly pure and complete dataset is flux-limited at $r < 20$ mag, covers ~ 1000 deg^2, and contains about 1 million galaxies after artifact masking. We exploit the overlap with Galaxy And Mass Assembly (GAMA) spectroscopy as calibration to determine photo-zs with the supervised machine learning neural network algorithm implemented in the ANNz2 software. The photo-zs have a mean error of $|\langle \delta z \rangle| \sim 5 \times 10^{-4}$ and low scatter (scaled mean absolute deviation of $\sim 0.018(1 + z)$); they are both practically independent of the r-band magnitude and photo-z at $0.05 < z_{phot} < 0.5$. Combined with the 9-band photometry, these allow us to estimate robust absolute magnitudes and stellar masses for the full sample. As a demonstration of the usefulness of these data, we split the dataset into red and blue galaxies, used them as lenses, and measured the weak gravitational lensing signal around them for five stellar mass bins. We fit a halo model to these high-precision measurements to constrain the stellar-mass–halo-mass relations for blue and red galaxies. We find that for high stellar mass ($M_\star > 5 \times 10^{11} M_\odot$), the red galaxies occupy dark matter halos that are much more massive than those occupied by blue galaxies with the same stellar mass. The data presented here are publicly released via the KiDS webpage at http://kids.strw.leidenuniv.nl/DR4/brightsample.php.

Key words. Galaxies: distances and redshifts – Catalogs – Large-scale structure of Universe – Gravitational lensing: weak – Methods: data analysis

1. Introduction

Galaxies are not distributed randomly throughout the Universe: they trace the underlying dark matter distribution, which itself forms a web-like structure under the influence of gravity in an expanding universe. For a given cosmological model, the growth of a structure can be simulated using cosmological numerical simulations, and the statistical properties of the resulting matter distribution as a function of scale and redshift can thus be robustly predicted. Given a prescription that relates their properties to the matter distribution, the observed spatial distribution of galaxies can thus be used to infer cosmological parameter estimates (e.g., Percival et al. 2001; Cole et al. 2005; Alam et al. 2017, 2021).

The galaxy redshift is a key observable in such analyses, and large spectroscopic surveys have therefore played an important role in establishing the current cosmological model. For large-scale clustering studies, it is advantageous to target specific subsets of galaxies rather sparsely because the survey can cover larger areas more efficiently. Consequently, most current results are based on redshift surveys that target specific galaxy types, such as luminous red galaxies (LRGs; Dawson et al. 2013; Blake et al. 2016). The downside of such strategies, however, is that detailed information about the environment is typically lost.

In contrast, a highly complete spectroscopic survey can only cover relatively small areas because fiber collisions or slit overlaps prevent or limit simultaneous spectroscopy of close galaxies; repeat visits are required to achieve a high completeness. For studies of galaxy formation and evolution, this can nonetheless be fruitful, as the Galaxy And Mass Assembly survey (GAMA, Driver et al. 2011) has demonstrated (e.g., Gunawardhana et al.

⋆ e-mail: bilicki@cft.edu.pl
⋆⋆ e-mail: dvornik@astro.ruhr-uni-bochum.de
⋆⋆⋆ e-mail: hoekstra@strw.leidenuniv.nl

2011; Robotham et al. 2011; Baldry et al. 2012). Although many of these applications rely on spectroscopic redshifts, several questions can still be addressed with less precise (photometric) redshift information over large areas.

To study the connection between galaxy properties and the dark matter distribution around galaxies, weak gravitational lensing has become an important observational tool. The foreground galaxies, which are embedded in dark matter dominated halos, act as lenses that distort space-time around them, leading to correlations in the shapes of more distant galaxies. This so-called (weak) galaxy-galaxy lensing (GGL) is used to study the stellar-mass–halo-mass relation (e.g., Leauthaud et al. 2012; Coupon et al. 2015; van Uitert et al. 2016) to examine the galaxy bias (e.g., Hoekstra et al. 2002; Dvornik et al. 2018), or to test modified gravity theories (e.g., Tian et al. 2009; Brouwer et al. 2017). Combined with measurements of the clustering of galaxies and the cosmic shear signal, so-called 3×2pt analyses provide competitive constraints on cosmological parameters (e.g., Abbott et al. 2018; Joudaki et al. 2018; van Uitert et al. 2018; Heymans et al. 2021). These applications rely on an overlapping sample of lenses with precise redshifts and a background sample with a large number of distant sources with reliable shape measurements. The latter are improving thanks to large, deep, multiband imaging surveys that cover increasingly larger areas of the sky, with the aim of measuring cosmological parameters using weak gravitational lensing, such as the Kilo-Degree Survey (KiDS, de Jong et al. 2013), the Dark Energy Survey (DES, The Dark Energy Survey Collaboration 2005), and the Hyper-Suprime Cam Subaru Strategic Program (Aihara et al. 2018).

In this paper we focus on KiDS, which covers 1350 deg^2 in nine broadband filters at optical and near-infrared (NIR) wavelengths. Unfortunately, the spectroscopic samples that overlap with the survey only yield ∼ 110 lenses per square degree in the case of the Baryon Oscillation Spectroscopic Survey (BOSS, Dawson et al. 2013), and ∼ 40 deg^{-2} for the 2-degree Field Lensing Survey (2dFLenS, Blake et al. 2016). They jointly cover the full final KiDS area of 1350 deg^2, and they have been exploited to test general relativity (Amon et al. 2018; Blake et al. 2020) and to constrain cosmological parameters (Joudaki et al. 2018; Heymans et al. 2021; Tröster et al. 2021), but their low number density limits the range of applications.

In contrast, GAMA provides a much denser sampling of up to 1000 lenses per deg^2 (albeit at a lower mean redshift than BOSS or 2dFLenS), allowing for unique studies of the lensing signal as a function of environment (e.g., Sifón et al. 2015; Viola et al. 2015; Brouwer et al. 2016; van Uitert et al. 2017; Linke et al. 2020), but its overlap with KiDS is limited to ∼ 230 deg^2. Hence for studies of the small-scale lensing signal, or studies of galaxies other than LRGs, we cannot rely on spectroscopic-only coverage over the full KiDS survey area. Fortunately, for many applications less precise photometric redshifts (photo-zs) suffice (e.g., Brouwer et al. 2018), provided that the actual lens redshift distribution is accurately known.

In Bilicki et al. (2018, B18 hereafter), we used the third KiDS data release (DR3, de Jong et al. 2017) covering 450 deg^2 and showed that by applying a limit of $r \lesssim 20$ to the imaging data, it was possible to extract a galaxy sample with a surface number density of ∼ 1000 deg^{-2} at a mean redshift $\langle z \rangle = 0.23$. Taking advantage of the overlap with GAMA spectroscopy, and using optical-only photometry (*ugri*) available from KiDS DR3, we obtained photo-zs that had a negligible bias with $\langle \delta z \rangle \sim 10^{-4}$ and a small scatter of $\sigma_{\delta z/(1+z)} \sim 0.022$. These redshift statistics were achieved by deriving photo-zs using a supervised machine-learning (ML) artificial neural net-

works (ANN) algorithm (ANNz2, Sadeh et al. 2016), which was trained on galaxies with spectroscopic redshifts (spectro-zs) in common between KiDS and GAMA. Such a good photo-z performance was possible thanks to the very high spectroscopic completeness of GAMA in its three equatorial fields (G09, G12, & G15): at the limit of $r < 19.8$, only ∼ 1.5% of the targets (preselected from SDSS) do not have a spectroscopic redshift measured there (Liske et al. 2015). As GAMA is essentially a complete subset of the much deeper KiDS dataset, restricting the latter to the flux limit of the former allowed us to take full advantage of the main supervised ML benefit: if a well-matched training set is available, then photo-zs derived with this technique is accurate and precise.

Here we extend the successful analysis of B18 to a larger area and broader wavelength coverage using the imaging data from the fourth public KiDS data release (DR4; Kuijken et al. 2019). We improve upon the earlier results and derive statistically precise and accurate photo-zs for a flux-limited sample of bright galaxies without any color preselection. The imaging data cover about 1000 deg^2 in nine filters, combining KiDS optical photometry with NIR data from the VISTA Kilo-degree Infrared Galaxy survey (VIKING, Edge et al. 2013). As shown in B18, the addition of the NIR data should improve the photo-z performance with respect to the earlier work. Following that previous study, we take advantage of the overlapping spectroscopy from GAMA, which allows for a robust empirical calibration. This leads to better individual redshift estimates for bright, low redshift galaxies, both in terms of lower bias and reduced scatter, compared to the default photo-z estimates that are provided as part of KiDS DR4. Those photo-zs were derived with the Bayesian Photometric Redshift approach (BPZ; Benítez 2000), with settings optimized for relatively faint ($r > 20$) and high-z cosmic shear sources, which makes them suboptimal for bright, low-redshift galaxies (B18; Vakili et al. 2019).

Over the full KiDS DR4 footprint of ∼ 1000 deg^2, we selected a flux-limited galaxy sample, closely matching the GAMA depth ($r < 20$), and we derived photo-zs for all the objects with 9-band detections. We call this sample KiDS-Bright for short. The final catalog includes about a million galaxies after artifact masking, that is ∼ 1000 objects per square degree. The inclusion of the NIR photometry reduces the photo-z scatter to $\sigma_{\delta z/(1+z)} \sim 0.018$, whilst still retaining a very small bias of $|\langle \delta z \rangle| < 10^{-3}$.

As a further extension of the previous results (B18), we derived absolute magnitudes and stellar masses for the KiDS-Bright sample, using the LePhare (Arnouts et al. 1999; Ilbert et al. 2006) spectral energy distribution fitting software. As an example of a scientific application of this dataset, we present a study of the stellar-to-halo-mass relation using GGL, where we split the sample into blue and red galaxies.

This paper is organized as follows. In Sect. 2 we describe the data used: KiDS in Sect. 2.1, GAMA in Sect. 2.2, and the selection of the KiDS-Bright sample in Sect. 2.3. In Sect. 3 we present the photometric redshift estimation, quantify the photo-z performance (Sect. 3.1), and provide a model for redshift errors (Sect. 3.2). In Sect. 4 we discuss the stellar mass and absolute magnitude derivation, validate it with GAMA, and provide details of the red and blue galaxy selection. We present the GGL measurements using this sample in Sect. 5, compare them to the signal from GAMA in Sect. 5.1, and use them to constrain the stellar-to-halo mass relation in Sect. 5.2. We conclude in Sect. 6.

The paper is accompanied by the public release of the data presented here[1], including the photo-zs and estimates of physical properties for the full KiDS-Bright galaxy sample over the $\sim$ 1000 deg^2 footprint of KiDS DR4.

2. Data and sample selection

2.1. KiDS imaging data

To select our galaxy sample, we used photometry in nine bands from a joint analysis of KiDS ($ugri$) and VIKING ($ZYJHK_s$) data that form the fourth public KiDS data release (Kuijken et al. 2019)[2]. This combined data set, which we refer to as "KV", covers an area of approximately 1000 deg^2, limited by the KiDS 4-band observations obtained by January 24, 2018 (VIKING had fully finished earlier). KiDS imaging was obtained with the OmegaCAM camera (Kuijken 2011) at the VLT Survey Telescope (Capaccioli et al. 2012), while VIKING employed the VIRCAM (Dalton et al. 2006) on the Visible and Infrared Survey Telescope for Astronomy (VISTA, Emerson et al. 2006).

The imaging data were processed using dedicated pipelines: the Astro-WISE information system (McFarland et al. 2013) for the production of co-added images ("coadds") in the four optical bands, and a THELI (Erben et al. 2005) r-band image reduction to provide a source catalog suitable for the core weak lensing science case. The VIKING magnitudes for KiDS DR4 were obtained from forced photometry on the THELI-detected sources, using a re-reduction of the NIR imaging that started from the VISTA "paw-prints" processed by the Cambridge Astronomical Survey Unit (CASU).

Photometric redshift estimates rely on robust colors, for which we use the Gaussian Aperture and Photometry (GAaP, Kuijken 2008) measurements, which in DR4 are provided for all the bands. They are obtained via a homogenization procedure in which calibrated and stacked images are first "Gaussianized," that is the point-spread-function (PSF) is homogenized across each individual coadd. The photometry is then measured using a Gaussian-weighted aperture (based on the r-band ellipticity and orientation) that compensates for seeing differences between the different filters (see Kuijken et al. 2015 for more details). Our ML photo-z derivation requires that magnitudes are available in all of the filters employed. Hence we require that the sources have data and detections in all nine bands.

The GAaP magnitudes are useful for accurate color estimates, but they miss part of the flux for extended sources. Various other magnitude estimates are, however, provided for the r-band data. Here we use the Kron-like automatic aperture MAG_AUTO and the isophotal magnitude MAG_ISO, as measured by SExtractor (Bertin & Arnouts 1996). These are not corrected for Galactic extinction and zero-point variations between different KiDS tiles (unlike the published GAaP magnitudes). To account for this, we define $r_{\rm auto}^{\rm KiDS} = $ MAG_AUTO + DMAG $-$ EXTINCTION_R (and analogously for MAG_ISO), where DMAG are per-tile zero-point offset corrections, and the Galactic extinction at the object position was derived from the Schlegel et al. (1998) maps with the Schlafly & Finkbeiner (2011) coefficients. Where unambiguous, we do not use the "KiDS" superscript.

In order to separate galaxies from stars, we used three star-galaxy separation indicators provided in the KiDS DR4 multiband dataset. The first one is the continuous CLASS_STAR de-

rived with SExtractor, ranging from 0 (extended) to 1 (point sources). The second separator is the discrete SG2DPHOT classification bitmap based on the r-band detection image source morphology (e.g., de Jong et al. 2015), which for instance is set to 0 for galaxies and 1, 4, or 5 for stars. Lastly, also SG_FLAG is a discrete star-galaxy separator that is equal to 0 for high-confidence stars and 1 otherwise[3].

The catalogs contain two flags that can be used to identify problematic sources (artifacts). The first one is IMAFLAGS_ISO, a bitmap of mask flags indicating the types of masked areas that intersect with the isophotes of each source, as identified by the PULECENELLA software (de Jong et al. 2015). We require this flag to be 0. The second flag is the KV multiband bit-wise MASK, which combines Astro-WISE and THELI flags for the KiDS and VIKING bands[4]. It indicates issues with source extraction, such as star halos, globular clusters, saturation, and chip gaps. The recommended selection in DR4 is to remove sources with (MASK&28668) > 0. We did not apply this mask by default in the final dataset, but instead we provide a binary flag indicating whether an object meets this masking criterion or not.

In Section 5 we explain how we measured the lensing signal around our sample of bright galaxies using shape measurements that are based on the r-band images. The galaxy shapes were measured using *lens*fit (Miller et al. 2013), which was calibrated with image simulations described in Kannawadi et al. (2019). Those are complemented with photo-z estimates based on an implementation of the BPZ code (Benítez 2000). For further details on the image reduction, photo-z calibration, and shape measurement analysis for these background sources, we refer the interested reader to Kuijken et al. (2019); Giblin et al. (2021), and Hildebrandt et al. (2021).

2.2. GAMA spectroscopic data

The Galaxy And Mass Assembly survey (Driver et al. 2011) is a unique spectroscopic redshift and multiwavelength photometric campaign, which employed the AAOmega spectrograph on the Anglo-Australian Telescope to measure galaxy spectra in five fields with a total $\sim$ 286 deg^2 area. Four of these fields (equatorial G09, G12, and G15 of 60 deg^2 each, and Southern G23 of $\sim$ 51 deg^2) fully overlap with KiDS, and we exploited this to optimize the bright galaxy selection and calibrate the photo-zs. Unique features of GAMA include the panchromatic imaging, spanning almost the entire electromagnetic spectrum (Driver et al. 2016; Wright et al. 2016), and the detailed redshift sampling in its equatorial fields: it is 98.5% complete for SDSS-selected galaxies with $r < 19.8$ mag, providing an almost volume-limited selection at $z \lesssim 0.2$, and it includes a sizable number of galaxies up to $z \sim 0.5$.

In our work we use the "GAMA II" galaxy dataset (Liske et al. 2015) from the equatorial fields, which includes, but is not limited to, the first three public GAMA data releases. The GAMA targets for spectroscopy were selected there from SDSS DR7 imaging (Abazajian et al. 2009), requiring a Petrosian (1976) magnitude $r_{\rm Petro} < 19.8$. Only extended sources were targeted, primarily based on the value of $\Delta_{sg} = r_{\rm psf} - r_{\rm model}$ (Strauss et al. 2002), where the two latter magnitudes are the SDSS PSF and model r-band measurements, respectively. To improve the point source removal further, the $J - K$ NIR color from the

---

[1] Data will be available upon publication. Please contact the authors for earlier access.
[2] See http://kids.strw.leidenuniv.nl/DR4/index.php for data access.

[3] See Kuijken et al. (2015) sect. 3.2.1 for a description of this star-galaxy separation.
[4] See http://kids.strw.leidenuniv.nl/DR4/format.php#masks for details.

UKIRT Infrared Deep Sky Survey (UKIDSS, Lawrence et al. 2007) was also used (Baldry et al. 2010).

In the equatorial fields, GAMA also includes sources fainter than $r = 19.8$ and/or selected differently than the main flux limited sample ("filler" targets; see Baldry et al. (2010); Liske et al. (2015); Baldry et al. (2018) for details). We used these in the KiDS photo-z training together with the flux-limited sample, but not to calibrate the bright-end selection. KiDS also overlaps with the southern G23 field, but the targets there were selected at a brighter limit ($i < 19.2$) than in the equatorial areas, and they were observed at a lower completeness. We therefore did not use that field for our sample selection and photo-z calibration.

We used the equatorial fields of GAMA TilingCatv46, which cover roughly 180 deg^2 fully within the KiDS DR4 footprint. To ensure robust spectroscopy, we required a redshift quality[5] NQ ≥ 3 and limited the redshifts to $z > 0.002$ to avoid residual contamination by stars or local peculiar velocities. Thus cross-matching selected GAMA with KV imaging data yields over 189 000 sources with a mean redshift of $\langle z \rangle = 0.23$. When unambiguous, by "GAMA," from now on we mean this selection of GAMA galaxies in the equatorial fields.

A small fraction (~ 4500 in total) of GAMA galaxies do not have counterparts in the KiDS multiband catalog. About 1300 of these are located at the edges of the GAMA fields, where KV coverage did not reach. The rest are scattered around the equatorial fields and include a considerable fraction of $z < 0.1$ galaxies, of low surface brightness galaxies, and of GAMA filler targets. These missing objects should not affect the analysis presented in this paper.

In Sect. 4 we use the stellar mass estimates of GAMA galaxies for a comparison with our results from the KiDS-Bright catalog. For this we employ the StellarMassesLambdarv20 dataset, which includes physical parameters based on stellar population fits to rest-frame u-Y SEDs, using Lambda Adaptive Multi-Band Deblending Algorithm in R (LAMBDAR, Wright 2016) matched aperture photometry measurements of SDSS and VIKING photometry (Wright et al. 2016) for all $z < 0.65$ galaxies in the GAMA-II equatorial survey regions. This sample contains over 192 000 galaxies, with a median $\log(M_\star/M_\odot) \sim 10.6$ assuming $H_0 = 70 \, \mathrm{km \, s^{-1} \, Mpc^{-1}}$, and a range between the 1st and 99th percentile of $(8.4; 11.2)$ in the same units. Here and below by "log," we mean the decimal logarithm, $\log_{10}$. For further details on the GAMA stellar mass derivation, see Taylor et al. (2011) and Wright et al. (2016).

2.3. KiDS-Bright galaxy sample

To ensure that the highly complete, flux-limited GAMA catalog is the appropriate photo-z training set for the KiDS-Bright sample, the selection of the latter should mimic that of the former as closely as possible. The differences between the KiDS and SDSS photometry, filter transmission curves, as well as the data processing of both surveys prevent an exact matching. In particular, Petrosian magnitudes were not measured by the KiDS pipeline; even if they had been though, the different r-band PSF (sub-arcsecond in KiDS versus median ~ 1.3" in SDSS,) and depth (~ 25 mag of KiDS versus ~ 22.7 in SDSS) would mean that the sources in common would on average have a much higher
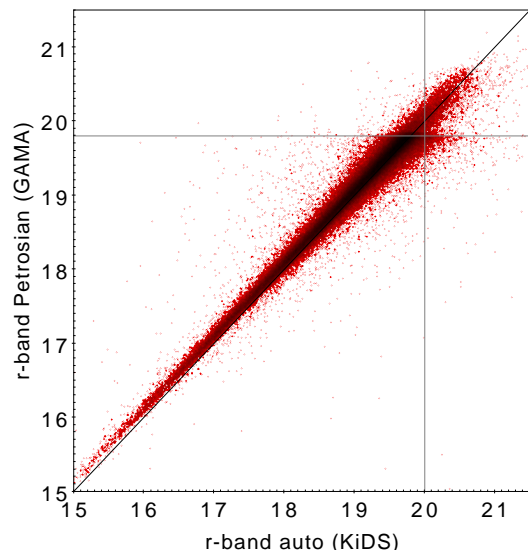
signal-to-noise in KiDS. Due to the photometric noise (Eddington bias, etc.), even applying the same cut to the same magnitude type (if possible) would not result in the same selection for the two surveys.

Instead, we used the overlap with GAMA and designed an effective bright galaxy selection from KiDS, aiming at a trade-off between completeness and purity of the dataset. To select only extended sources (galaxies), we verified how the three star-galaxy separation metrics available in KiDS DR4 (`CLASS_STAR`, `SG2DPHOT` and `SG_FLAG`) perform for the GAMA sources. We found that the optimal approach is to jointly apply the following conditions: `CLASS_STAR < 0.5` & `SG2DPHOT = 0` & `SG_FLAG = 1`. These remove less than 0.5% of the matched KiDS×GAMA $r_{\mathrm{Petro}} < 19.8$ galaxies, so this selection ensures a completeness of more than $\sim 99.5\%$.

As far as the magnitude limit of the KiDS-Bright galaxy selection is concerned, we verified which of the r-band magnitude types – `AUTO` or `ISO` – is the most appropriate for the selection. We find that `ISO` matches the SDSS Petrosian magnitude slightly better: the median difference $\Delta_{\mathrm{iso}} \equiv r_{\mathrm{iso}}^{\mathrm{KiDS}} - r_{\mathrm{Petro}}^{\mathrm{GAMA}} \simeq -0.02$ as compared to $\Delta_{\mathrm{auto}} \simeq -0.06$. However, the scatter in Δ_{auto} is smaller than in Δ_{iso}: the former is more peaked (i.e., narrower interquartile and 10- to 90-percentile ranges around the median) than the latter. We therefore decided to use $r_{\mathrm{auto}} < 20$ for the bright sample selection. This ensures a completeness level of over 99% with respect to the GAMA $r < 19.8$ selection.

Figure 1 presents a comparison of the SDSS Petrosian and KiDS `AUTO` r-band magnitudes for the galaxies in common with GAMA, including those beyond the completeness limit of the latter. The vertical and horizontal gray lines show the GAMA flux limit and the cut we adopted for the selection of the KiDS-Bright galaxy sample, respectively. The combination of $r_{\mathrm{auto}} < 20$ and the star removal results in an incompleteness in the galaxy selection of $\sim 1.2\%$ with respect to GAMA.

Quantifying the purity of the resulting KiDS-Bright sample is more challenging as this formally requires a complete flux-limited sample of spectroscopically confirmed galaxies, quasars,

Fig. 1. Comparison between the KiDS r_{auto} and the Petrosian r-band from SDSS for galaxies in common between the two data sets. The GAMA selection is based on the latter magnitude, whereas we used the former to determine the flux limit of our galaxy sample. The relevant magnitude limits are indicated with the gray lines, and the black diagonal is the identity line.

---

[5] GAMA galaxies with NQ < 3 are often fainter than the completeness limit, so in principle they could be helpful in the KiDS-Bright sample selection and calibration. However, their redshifts have lower than a 90% probability of being correct (Liske et al. 2015), and they are not recommended for scientific applications.

and stars deeper than GAMA. As such a dataset is not available at present, we assess the purity using indirect methods instead. Possible contaminants are artifacts, incorrectly classified stars, or quasars for which galaxy photo-zs may be inaccurate (especially if at high-z).

A small fraction of the bright sources have nonphysical or otherwise spurious photo-zs (derived as described in Sect. 3), that is $z_{phot} < 0$ or $z_{phot} > 1$; these constitute only $\sim 0.05\%$ of the sample after applying the default mask. The stellar contamination should be minimal as we combined three flags for galaxy selection, which should yield a robust classification for objects detected with a high signal-to-noise ratio. Indeed, a cross-match with the SDSS DR14 spectroscopic star sample (Abolfathi et al. 2018) yields only 170 matches out of $\sim 50\,000$ SDSS stars in the KiDS-North area; extrapolated to KiDS-South, this would imply a contamination of this type of at most 0.05%. Although SDSS stars do not constitute a uniform and flux limited sample at this depth, this still supports our expectation that the star contamination should be negligible. We also do not expect quasars to be significant and problematic contaminants: a similar cross-match, but with SDSS DR14 spectroscopic quasars, results in about 650 common sources, of which 90% have $z_{spec} < 0.5$. Matching the KiDS-Bright data with a much more complete, photometrically selected sample of KiDS quasars derived by Nakoneczny et al. (2021), which covers the whole DR4 footprint, gives ~ 1400 common objects, of which 90% have $z_{phot}^{QSO} < 0.66$ (the "QSO" superscript refers to the quasar photo-z as derived in that work). Both of these tests suggest that the possible contamination with high-z quasars is also a fraction of a percent. The photo-zs of such residual quasars are worse than for the general galaxy sample, but the very small number of them does not influence the overall statistics and the quality of the dataset.

Finally we examine the impact of KiDS-Bright objects that are fainter than the completeness limit of GAMA, that is they have $r_{Petro} > 19.8$ (see Fig. 1). Following the analysis above, these are most likely galaxies, and as such should not be considered contaminants, but they are not well represented by the GAMA spectroscopic sample or, alternatively, not represented at all. The photo-z estimates of such galaxies could be affected by the fact that their calibration is based on the incomplete and nonuniform sampling of GAMA filler targets beyond the nominal flux limit of the survey. On the other hand, the KiDS-Bright objects beyond the GAMA limit, but with colors similar to those included in the flux-limited spectroscopic sample, should still attain reliable photo-zs.

One way to estimate the number of such faint-end sources is to compare the catalogs for the GAMA equatorial fields. After all the selections, the KiDS-Bright sample comprises less than $192\,000$ galaxies, whereas the GAMA sample, with $r_{Petro} < 19.8$, contains more than $182\,000$ objects. The difference of approximately 9000 objects provides an upper limit of $\sim 4.7\%$ for galaxies that are not fully represented in the GAMA catalog. The true fraction is likely below this number because only galaxies with misestimated photo-zs based on extrapolation beyond GAMA should be considered as potentially problematic. Their number is difficult to estimate without a comparison against a complete flux-limited galaxy spectroscopic sample, deeper than GAMA and overlapping with KiDS. Such a dataset is presently unavailable; we can, however, estimate how many of the KiDS-Bright galaxies are similar to GAMA "filler" targets. In the cross-matched KiDS×GAMA sample, there are about 4800 GAMA fillers with $r_{Petro} > 19.8$ out of the ~ 146k selected in the same way as the KiDS-Bright ($r_{auto} < 20$ plus the galaxy selections and masking detailed above); this yields about 3.3%. The photo-

z performance of such a filler sample is worse, but not catastrophic: their $\langle \delta z \rangle \simeq 1.6 \times 10^{-3}$ and $\sigma_z \simeq 0.024(1 + z)$ at a mean redshift of $\langle z \rangle = 0.33$. For those KiDS-Bright galaxies which are not represented in GAMA at all, we cannot reliably estimate the overall photo-z performance: deeper spectroscopic samples overlapping with KiDS are not sufficiently complete.

To summarize, we estimate that the KiDS-Bright sample has a very high purity level close to 100%, as contamination from stars, high-redshift quasars, or artifacts is at a small fraction of a percent. There is, however, an inevitable mismatch with GAMA flux-limited selection, with up to 3% of the galaxies in KiDS-Bright not being fully represented by GAMA spectroscopy. These could potentially have photo-zs based on ML extrapolation that are less reliable.

3. Photometric redshifts

To obtain photo-z estimates that are optimized for our sample of bright low-redshift galaxies, we took advantage of the large amount of spectroscopic calibration data. To do so, we used supervised ML in which a computer model (based on ANNs in our case) learns to map the input space of "features" (magnitudes) to the output (redshift) based on training examples, which in our case are the KiDS galaxies with a GAMA spectro-z. The trained model was subsequently applied to the entire "inference" dataset, which in our case is the galaxy sample selected as described in Sect. 2.3.

Similarly to B18, we used the ANNz2 software[6] (Sadeh et al. 2016) to derive the photo-zs for the KiDS-Bright galaxy sample. This package implements a number of supervised ML models for regression and classification. Throughout this work, we employed ANNz2 in the "randomized regression" mode, in which a preset number (here: 100) of networks with randomized configurations is generated for each training, and a weighted average is provided as the output. We trained ANNs using the GAMA-II equatorial sources that overlap with KiDS DR4. We verified that adding the Southern GAMA G23 data does not improve the final photo-z statistics – G23 is shallower and less complete than the equatorial data, and including it does not add any new information in the feature space that the networks could use to improve the photo-z performance. For similar reasons, we did not employ other wide-angle spectroscopic data, such as SDSS or 2dFLenS, to the training set. Those samples include flux-limited subsets shallower and less complete than GAMA, while at the fainter end they encompass only color-selected galaxies, mostly red ones, which if employed in photo-z training, would bias the estimates against blue sources.

The galaxies were used in various configurations for the photo-z training, validation, and tests. To enable some level of extrapolation by the ML model in the range of $r_{Petro} > 19.8$ & $r_{auto} < 20$ (see Fig. 1), we did not limit them to the GAMA completeness cut. As the ANNs in our setup cannot handle missing data, we require photometry in all nine bands, also for the tests we discuss below. However, as the galaxies are much brighter than the magnitude limits of both KiDS and VIKING, we only lose ~ 1500 objects out of a total of $189\,000$ spectroscopic galaxies.

In the testing phase, we randomly selected 33% of the galaxies with redshifts from GAMA as a joint training and validation set, while the rest were used for testing. In all cases, the actual

---

[6] Available for download from https://github.com/IftachSadeh/ANNZ. We used version #2.3.1.
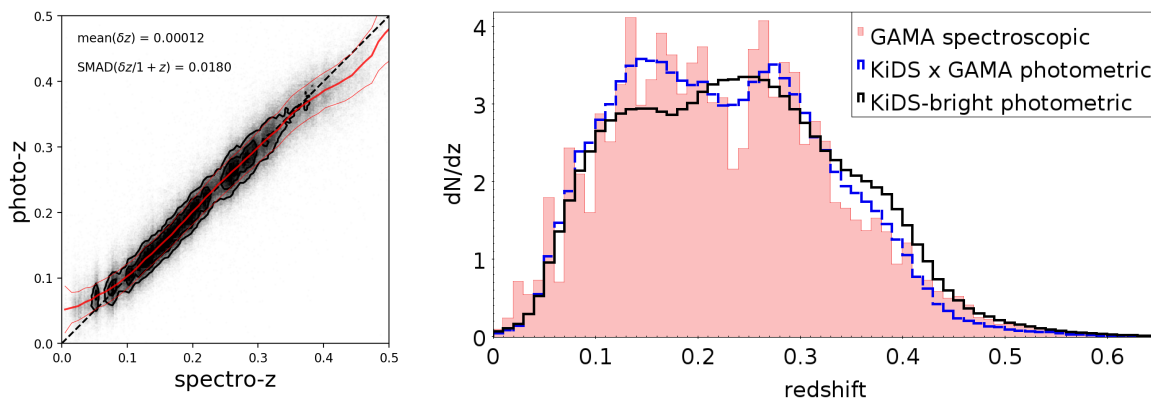
Fig. 2. Comparison of the KiDS-Bright photometric redshifts with the overlapping GAMA spectroscopic data. *Left:* Direct spectro-z – photo-z comparison. The thick red line is the running median of the function $z_{phot}(z_{spec})$ and the thin red lines illustrate the scatter (SMAD) around the median. The black dashed line shows the identity. *Right:* Comparison of redshift distributions of the GAMA spectroscopic training set (red bars), photo-zs for the common KiDS×GAMA sources (blue dashed line), and the full KiDS-Bright photo-z sample (black line). The histograms are normalized to the unit area.

validation set (used internally by ANNz2 for network optimization) was randomly selected as half of the input training and validation sample. For the final training of the photo-zs of our bright galaxies, we used the entire cross-matched sample, again with a random half-half split for actual training and validation (optimization) in ANNz2. As shown in B18, these proportions between training, validation, and test sets can be varied within reasonable ranges without much influence on the results; we dealt with sufficiently large samples to ensure robust statistics.

To evaluate the performance, we measured the "scatter," defined as the scaled median absolute deviation (SMAD) of the quantity $\Delta z \equiv \delta_z/(1 + z_{true})$ with $\delta_z \equiv z_{phot} - z_{true}$ and $SMAD(x) = 1.4826 \times median(|x - median(x)|)$. As z_{true}, we used the spectro-zs from the test sample. In B18 we showed that adding NIR VIKING magnitudes to the *ugri*-only setup available in KiDS DR3 reduced the scatter of the photo-zs at the GAMA depth by roughly 9%, from $\sigma_z \simeq 0.022(1 + z)$ to $0.020(1 + z)$. The VIKING measurements employed there were based on GAMA-LAMBDAR forced photometry (Wright et al. 2016), using SDSS apertures as input and without PSF corrections that are applied in KV processing (Wright et al. 2019; Kuijken et al. 2019). We therefore expect that the improved color measurements in DR4 should reduce the errors even further. Indeed, we find that the scatter of 9-band KiDS DR4 photo-zs for our bright galaxies is further reduced with respect to the KiDS DR3 + LAMBDAR VIKING statistics, in total by $\sim 18\%$ from the DR3 *ugri*-only derivation (see Table 1 below). We also verified that omitting any of the 9 bands worsens the performance. None of the VIKING bands stand out, which is expected, because for the redshifts covered by GAMA ($z < 0.5$), the NIR data do not trace clear features in the spectrum; rather they sample the Rayleigh-Jeans tail, and thus each of the VIKING bands adds a similar amount of information.

The photo-zs could be potentially improved if additional features are included in the training. In B18 we studied this in detail for a similar bright sample of galaxies, and found that adding colors (magnitude differences) and galaxy angular sizes (semi-axes of best-fit ellipses) did lead to better photo-z estimates, compared to the magnitude-only case. For the 9-band data, however, there are 36 possible colors and feeding the ANNs with all of them, together with the magnitudes, would be very inefficient without specific network optimization each time; some prior feature importance quantification to choose the most relevant sub-

set would be needed. This is beyond the scope of this work and therefore we limit the photo-z derivation to magnitudes only. Unlike B18, we decided not to use any size information because the available estimates are not PSF-corrected. Using the uncorrected sizes could introduce a systematic variation of photo-z quality with the PSF at a source position. As one of the applications of the KiDS-Bright sample is to use it for cosmological measurements, we decided to employ only the PSF-corrected GAaP magnitudes for redshift estimation.

As already mentioned in Sect. 2.1, each KiDS object is assigned a `MASK` flag, indicating issues with source extraction. The default masking, used to create the KiDS-1000 weak lensing mosaic catalogs, is to remove the sources matching bit-wise the value 28668. We checked the importance of this masking for photo-z quality by performing two ANN trainings: one including all the training sources with any mask flag, and another one where only the sources with the default masking were used. For each of the cases, the performance was evaluated using the same blind test set. We did not observe any difference between the photo-z statistics for the two training cases. Our interpretation is that the ANNs are able to "learn" the noise related to the `MASK` flag. By ignoring this flag in the training phase, they are still able to robustly estimate photo-zs. At the same time, as far as the evaluation is concerned, there is a clear deterioration in the photo-z performance for the sources that should be masked out with respect to those that pass the default selection, for both training setups. Motivated by these findings, we ignored the `MASK` value for the training set for the final sample. We however provide a flag with our photo-z estimates that indicates which of the galaxies meet the condition (`MASK` & 28668) > 0 and should be preferably masked out for science applications.

3.1. Photometric redshift performance

We compare the KiDS-Bright photo-zs with the overlapping spectro-zs from GAMA in Fig. 2. The left panel shows that the photo-zs are overestimated at low-z and underestimated at high-z, which is common for ML approaches. Nonetheless, the overall performance is excellent, with a low average bias and a small and near constant scatter as a function of redshift.

The redshift distributions presented in the right panel of Fig. 2 indicate that for the matched KiDS×GAMA galaxies, dN/dz_{phot} (blue dashed line) closely follows the general shape
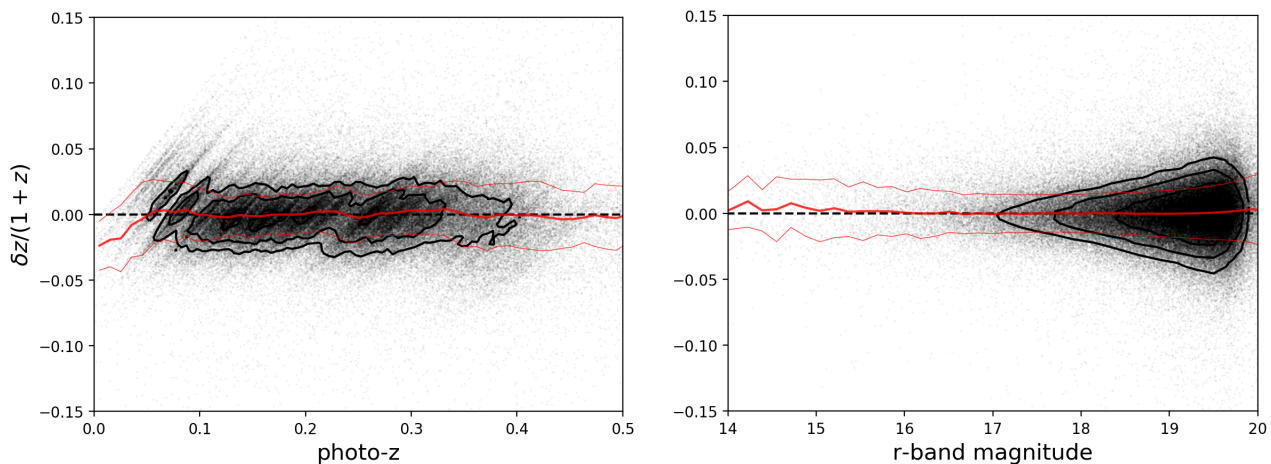
Fig. 3. Photometric redshift errors in the KiDS-Bright sample as a function of photo-z *(left)* and of the KiDS r-band AUTO magnitude *(right)*, calibrated on overlapping GAMA data. Each dot is a galaxy, with contours overplotted in the highest number density areas. The thick red line is the running median and the thin red lines illustrate the scatter (SMAD) around the median. The stripes in the left panel originate from the large-scale structures present in the GAMA fields.

of the true dN/dz_{spec} (red bars), preserving even the "dip" observed in GAMA at $z \sim 0.25$ (emerging by chance due to large-scale structures passing through the equatorial fields; e.g., Eardley et al. 2015). As far as the redshift distribution of the full photometric sample is concerned (black solid line), we observe some piling up of photo-zs at the very same range where the GAMA dip is present, but also at $z_{phot} \sim 0.35$. This might be the result of the extrapolation by ANNz2 in the regime $r_{auto} \sim 20$, where sources can be fainter than the GAMA completeness limit (Fig. 1), or for sources that are for some other reason underrepresented in GAMA (as discussed in Sect. 2.3).

To illustrate the KiDS-Bright photo-z performance in more detail, we show the redshift errors $\delta z/(1 + z)$ as a function of photo-z and r-band magnitude in Fig. 3. The errors show little dependence on the r-band magnitude or photometric redshift, except for the range $z_{phot} < 0.05$. Since at this redshift range the number density of the photometric KiDS galaxies is very small, and as it is additionally very well covered by wide-angle spectroscopic samples such as SDSS Main (Strauss et al. 2002), 6dFGS (Jones et al. 2009), and GAMA itself, this worse photo-z performance is irrelevant for scientific applications of the KiDS-Bright sample. We however recommend using only the $z_{phot} > 0.05$ sources; this cut affects less than 1% of the sample. At the high-redshift end of the dataset, $z_{phot} \gtrsim 0.4$, both the KiDS-Bright and GAMA calibration samples become very sparse (Fig. 2). However, the photo-z quality remains comparable to the rest of the dataset (Fig. 3), so the galaxies with $z_{phot} \lesssim 0.5$ should be safe for scientific applications once the flux-limited character of the sample is taken into account.

The fact that the photo-zs are practically unbiased as a function of the photo-z is typical for ML-based derivations, as the algorithms usually search for the best-fit solution for the photo-zs as calibrated on known spectro-zs. As the redshift distribution is not constant but has a well-defined maximum (especially for flux-limited samples such as ours), this then leads to an inevitable bias as a function of spectro-z at the extremes of the coverage, as already illustrated in Fig. 2. However, in most applications it is important to be able to select in photo-z and calibrate the true redshift distribution of a given sample a posteriori (e.g., in photo-z bins). For this, knowledge of the photo-z error

distribution (discussed below in Sect. 3.2) plus the dN/dz_{phot} are usually sufficient to build a reliable model.

The relative paucity of $z_{spec} \sim 0.25$ galaxies in the GAMA-equatorial data, used here for the photo-z training, is caused by a large-scale structure in these fields. This could potentially affect our redshift estimates if it was spuriously propagated by ANNz2. As we have already pointed out, this dip is correctly reproduced in the dN/dz_{phot} of the matched GAMA×KiDS sample, but it is not present in the overall photo-z distribution of the full KiDS-Bright sample. This suggests that the training is not significantly affected. As an additional test, we compared dN/dz_{spec} and dN/dz_{phot} of a cross-match between KiDS-Bright and spectroscopic redshifts in the Southern GAMA G23 field, in which such a lack of $z \sim 0.25$ sources is not observed. As mentioned earlier, the latter dataset was not used for the photo-z training because it is shallower and less complete than the GAMA-equatorial data. A comparison of the redshift histograms shows no spurious lack of photo-zs at $z \sim 0.25$. Nonetheless, close inspection of the left-hand panel of Fig. 3 does suggest some variation in photo-z performance in this range; a similar effect is also observed in a z_{spec} versus δz comparison. Such "wiggles" in the photo-z error as a function of redshift are still present if the G23 data are added to the ANNz2 training. However, for the current and planned applications of the KiDS-Bright sample, these issues are not significant. Nonetheless, this might need revisiting for future analyses with the full-area KiDS DR5 data.

Table 1 provides basic photo-z statistics for our KiDS-Bright sample. We list the total number of sources, their mean redshift, as well as photo-z bias and scatter (evaluated on overlapping GAMA spectroscopy). Comparison of the statistics for the full KiDS-Bright sample with that after masking demonstrates that masking improves the photo-z statistics somewhat; interestingly, it also slightly enlarges the mean redshift. We also report results when the sample is split by color based on the r-band absolute magnitude and the rest-frame $u - g$ color, derived with LePhare, as detailed in Sect. 4. With the adopted split, the red galaxies are slightly less numerous than the blue ones, but their photo-z performance is noticeably better.

For reference we also provide the results for the galaxies that overlap with the LRG sample from Vakili et al. (2020), but using our ANNz2 redshift estimates. This particular subsample stands

Table 1. Statistics of photometric redshift performance for the KiDS-Bright sample and selected subsamples. The sample sizes refer to the full photometric selection.

sample	number of galaxies	mean redshift	mean of $\delta z = z_{\rm ph} - z_{\rm sp}$	mean of $\delta z/(1 + z_{\rm sp})$	st.dev. of $\delta z/(1 + z_{\rm sp})$	SMAD of $\delta z/(1 + z_{\rm sp})$
full KiDS-Bright[a]	1.24×10^6	0.226	1.2×10^{-4}	6.7×10^{-4}	0.0246	0.0180
after masking[b]	1.00×10^6	0.229	4.6×10^{-4}	9.0×10^{-4}	0.0237	0.0178
red galaxies[c]	3.91×10^5	0.243	-2.7×10^{-4}	2.0×10^{-4}	0.0194	0.0159
blue galaxies[c]	4.25×10^5	0.212	1.5×10^{-3}	1.8×10^{-3}	0.0274	0.0200
luminous red galaxies[d]	7.18×10^4	0.305	1.1×10^{-3}	1.1×10^{-3}	0.0161	0.0141

Notes.
[a] Flux-limited galaxy sample ($r_{\rm AUTO} < 20$); see Sect. 2.3 for other details of the selection.
[b] Using the KiDS MASK flag, removing the sources meeting the condition (MASK&28668) > 0 (bit-wise).
[c] Selected using the r-band absolute magnitude and rest-frame $u - g$ color based on LePhare output; see Sect. 4 for details.
[d] Selected using the Bayesian model detailed in Vakili et al. (2020), jointly encompassing the "dense" and "luminous" samples. Numbers refer to the LRGs overlapping with the KiDS-Bright sample and the photo-z statistics are based on the ANNz2 derivations.

out with SMAD(Δz) ∼ 0.014, albeit with a slightly larger overall bias of $\langle \delta z \rangle \sim 10^{-3}$, which is still over an order of magnitude smaller than the scatter. These values are comparable to those obtained in Vakili et al. (2020) using the dedicated red-sequence model, which confirms the excellent quality of our photo-zs. The blue galaxies, despite performing worse overall in terms of their photo-z statistics, still have very well constrained redshifts with SMAD(Δz) ≃ 0.02. For the blue and red galaxies, we find similar trends as the ones presented in Fig. 3 for the full sample, albeit with different levels of scatter.

The quality of photo-zs can vary as a function of various survey properties. In Appendix A we present a short summary of the photo-z error variation for the KiDS-Bright sample versus a number of both KiDS-internal (PSF, background, and limiting magnitudes) and external (star density and Galactic extinction) observational effects. We find that both the photo-z bias and scatter are generally stable with respect to these quantities.

As mentioned earlier, the photo-z performance could potentially be improved if we additionally used galaxy colors, sizes, or other measurements correlated with redshift (e.g., B18). Some other avenues to explore here are to employ dedicated photometry, which is targeted better at apparently bright and large galaxies, such as those in our sample; this exists already for the GAMA fields (Bellstedt et al. 2020) and will be available for the entire KiDS footprint from the 4MOST WAVES team (Driver et al. 2019). One could also inspect other empirical photo-z methods, for instance the "scaled flux matching" (Baldry et al. 2021) or even deep learning techniques (e.g., Pasquet et al. 2019). We plan to study these aspects in the final KiDS data, as well as in the mocks resembling the KiDS-Bright sample (van den Busch et al. 2020), to verify how much improvement in the photo-zs we can still hope for.

3.2. Analytical model of the redshift errors

For a number of applications, such as angular clustering, GGL, or cross-correlations with other cosmological tracers, it is useful to have an analytical model of the photo-z errors, which can be used in theoretical predictions (e.g., Balaguera-Antolínez et al. 2018; Peacock & Bilicki 2018; Hang et al. 2021). The photometric redshift error distribution usually departs from a Gaussian shape due to a considerable number of several-σ outliers and generally broader "wings" (e.g., Bilicki et al. 2014; Pasquet et al. 2019; Beck et al. 2021). This is why SMAD, or alterna-
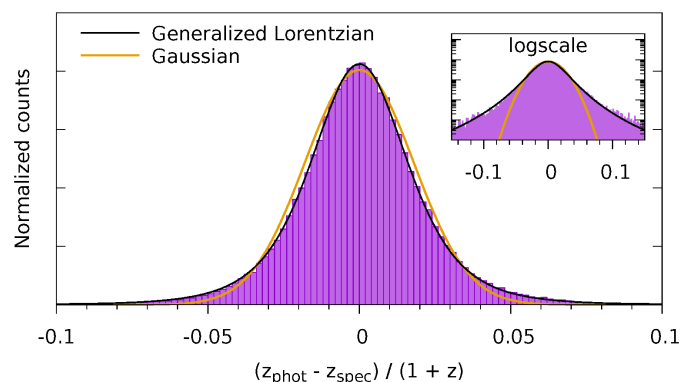

Fig. 4. Histogram of photometric redshift errors in the KiDS-Bright sample (magenta bars) fitted with a generalized Lorentzian (Eqn. 1, black line) with parameters $a = 2.613$ and $s = 0.0149$, compared to best-fit Gaussian (orange) with $\sigma = 0.0180$. The top-right inset elucidates the differences in the wings as seen in log-scaling.

tively percentiles (e.g., Wolf et al. 2017; Soo et al. 2018; Alarcon et al. 2021), are better suited to quantify the photo-z scatter than the standard deviation, which is sensitive to outliers. Functional forms to fit the empirical photo-z error distribution include the "modified Lorentzian" (Bilicki et al. 2014; Peacock & Bilicki 2018; Hang et al. 2021) or the Student's t-distribution (Vakili et al. 2020). The former is provided by (Bilicki et al. 2014)

$$N(\Delta z) \propto \left(1 + \frac{\Delta z^2}{2as^2} \right)^{-a}, \tag{1}$$

where we have assumed that the photo-zs are on average unbiased, which is a good approximation in our case as $\langle \Delta z \rangle \ll$ SMAD(Δz) (see Table 1). This can be easily generalized to the case of non-negligible bias by introducing an extra parameter (Hang et al. 2021). In Eqn. (1), the parameter s is related to the width of the distribution, while a encodes the extent of the wings. We note that both a and s can be parameterized as photo-z-dependent to build an analytical model of redshift error (Peacock & Bilicki 2018).

We used Eqn. (1) to fit the photo-z error distribution in the KiDS-Bright sample and find the best-fit parameters to be $a = 2.613$ and $s = 0.0149$. Qualitatively, this is indeed a very

good fit to the Δz histogram, as illustrated in Fig. 4, clearly outperforming the best-fit Gaussian with $\sigma = 0.0180$ (also assuming an average zero bias). The inset, with a log-scale to highlight the wings, shows that the Gaussian fails to account for the outliers. We do not quantify the goodness of fit of the two models as we do not have meaningful information on the errors on the Δz histogram.

Such an empirical shape for the photo-z error distribution could be the result of combining galaxy populations with different redshift precision, as illustrated in Table 1 for the red and blue selections. We have however verified that for both these galaxy subpopulations, selected as described in Sect. 4 below, their respective Δz distributions are also better fitted with the modified Lorentzian (1) than with a Gaussian. Similarly, as shown in Vakili et al. (2020), photo-zs for luminous red galaxies, albeit derived with a different approach, also display a non-Gaussian error distribution. This might indicate that such an error distribution is an inevitable outcome of at least some empirical photo-z methodologies.

4. Stellar masses & rest-frame absolute magnitudes

We estimate a number of rest-frame properties for each KiDS-Bright galaxy in the same manner as was done for the full-depth KV data within the DR3 footprint (KV450, Wright et al. 2019). We did this by fitting model spectral energy distributions (SEDs) to the 9-band GAaP fluxes of each galaxy using the LePhare (Arnouts et al. 1999; Ilbert et al. 2006) template fitting code. In these fits, we employed our ANNz2 photo-z estimates as input redshifts for each source, treating them as if they were exact. In practice, this has little influence on the fidelity of the stellar mass estimates (see Taylor et al. (2011)). We used a standard concordance cosmology ($\Omega_m = 0.3$, $\Omega_\Lambda = 0.7$, and $H_0 = 70 \, \mathrm{km \, s^{-1} \, Mpc^{-1}}$), a Chabrier (2003) initial mass function, the Calzetti et al. (1994) dust-extinction law, Bruzual & Charlot (2003) stellar population synthesis models, and exponentially declining star formation histories. The input photometry to LePhare was extinction corrected using the Schlegel et al. (1998) maps with the Schlafly & Finkbeiner (2011) coefficients, as described in Kuijken et al. (2019). For the optical VST bands, we utilized the filter profiles measured at the center of the field of view, available from the ESO webpages[7]. For the NIR VISTA data, we used the averaged filter profile of all 16 filter segments per band (Edge et al. 2013).

The LePhare code returns a number of quantities for each source, detailed in Appendix C. The best-fit MASS_BEST is the one that should be used as the estimate of galaxy's stellar mass; this quantity is available for almost all KiDS-Bright objects, except for a few hundred which have unreliable photo-zs (e.g., $z_{\mathrm{phot}} < 0$). When using these stellar mass estimates, it is however important to take into account the "flux scale correction" related to the fact that the GAaP magnitudes used by LePhare underestimate fluxes of large galaxies. The correction that we used is based on the difference between the AUTO and GAaP r-band magnitudes (see Eqn. C.1) and it was added to the logarithm of the stellar mass estimate given by MASS_BEST (Eqn. C.2).

The code also outputs MASS_MED, which is the median of the galaxy template stellar mass probability distribution function. This quantity can take a value of -99, which indicates that a galaxy was best-fit by a non-galaxy template; although, the MASS_BEST value still reports the mass from the best-fitting
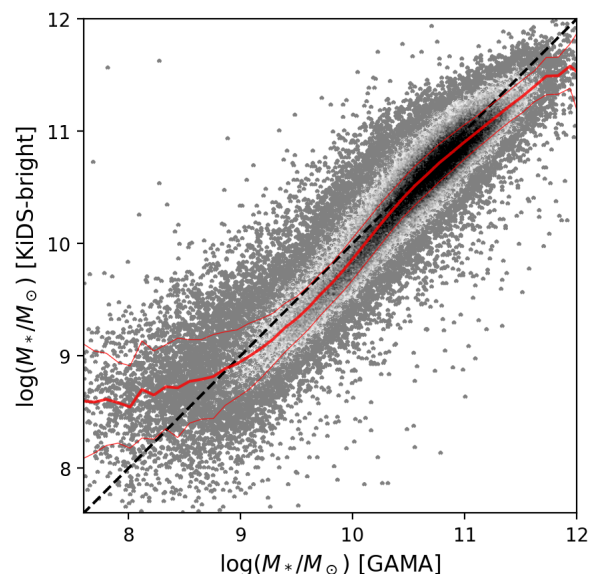
Fig. 5. Comparison of the derived stellar masses between the photometric KiDS-Bright sample (this work) and the spectroscopic GAMA dataset for galaxies common to both catalogs. The light gray to black scaling illustrates the bulk of the sample, while the outliers where the number density is smaller, are shown with individual large gray dots. The thick red line is the running median, and thin red lines illustrate the scatter (SMAD).

galaxy template. In some cases this could highlight stellar contamination for sources that are best-fit by a stellar template and additionally have a small flux radius, and this could be even used for star-galaxy separation (see the related discussion in Wright et al. 2019). This is, however, not a concern for our sample: out of over 270 000 objects with MASS_MED $= -99$, only a few lie on the stellar locus. This further confirms the very high purity level of the KiDS-Bright catalog, as already concluded in Sect. 2.3.

The median stellar mass of the KiDS-Bright sample is $\log(M_\star/M_\odot) \sim 10.5$, with a range between the 1st and 99th percentile of roughly $8.5 < \log(M_\star/M_\odot) < 11.4$. In order to assess the quality of these stellar mass estimates, we compared them with the GAMA stellar mass catalog (Taylor et al. 2011; Wright et al. 2016), introduced in Sect. 2.2. First of all, it is worth noting that the overall distributions of the stellar masses (normalized histograms of $dN/d(\log M_\star)$) are very similar, and in particular their maximum (mode) is at ~ 10.75 in both cases. Cross-matching the two samples gives about 145 000 galaxies with stellar masses from both KiDS-Bright and GAMA. We compare these directly in Fig. 5, where we also plotted the running median relation together with the corresponding SMAD (respectively thick and thin red lines). We see that the relation is within $\sim 1\sigma$ from the identity line (dashed) over a wide range in stellar mass and significantly departs from it only at the tails of the distribution. On average, the KiDS-Bright stellar mass estimates are smaller than those of GAMA by $\Delta \log M_\star \equiv \log M_*^{\mathrm{KiDS}} - \log M_*^{\mathrm{GAMA}} = -0.09 \pm 0.18$ dex (median and SMAD). Such an overall bias between the former and the latter is expected: while our flux-scale correction is meant to compensate for the flux missed by the GAaP measurements with respect to AUTO magnitudes, an analogous correction in GAMA serves to account for a flux that falls beyond the finite SDSS-based AUTO aperture used for the SEDs.
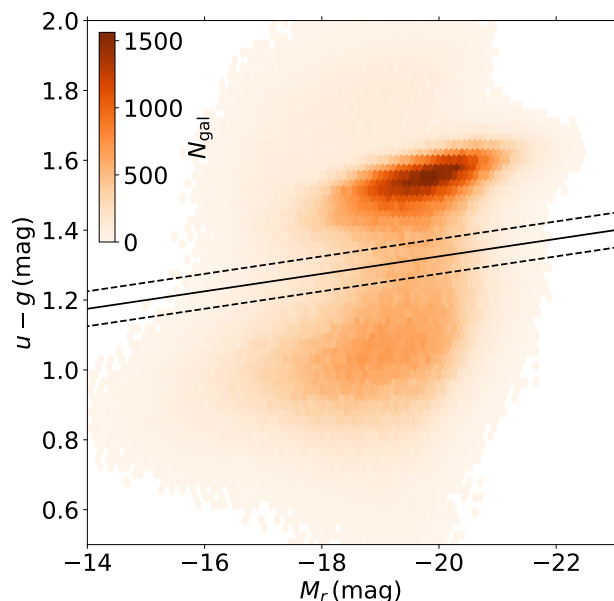
Fig. 6. Distribution of the $u - g$ rest-frame color versus absolute r-band magnitude for the KiDS-Bright galaxy sample, based on LePhare derivations with ANNz2 photo-zs as input redshifts. We used the location of the green valley to derive an empirical split into red and blue galaxies above the upper dashed and below the lower dashed lines, respectively.

Nonetheless, the overall consistency is remarkable, given that the stellar masses were determined using different data and methodology: GAMA employed spectroscopic redshifts together with LAMBDAR photometry from SDSS+VIKING u to Y bands, while we used photo-zs and GAaP KiDS+VIKING u to K_s measurements. While the GAMA stellar masses cannot be treated as the "ground truth" due to inevitable systematics in the modeling, it is worthwhile to explore trends in the stellar mass differences between the two data sets. We observe no significant trend of $\Delta \log M_\star$ with magnitude or with color. Not surprisingly, the use of photo-zs does affect the performance for galaxies, especially at very low redshifts ($z_\text{spec} \lesssim 0.07$).

In general, we observe a linear trend in $\Delta \log M_\star$ with $\delta z/(1+z)$. If we account for this trend, the SMAD in $\Delta \log M_\star$ is ~ 0.17 dex, that is $\sim 9\%$ lower than for the entire matched sample; this difference can be regarded as the effective increase in the scatter between GAMA and KiDS-Bright stellar mass derivations due to the photo-zs only. Overall, we find that the results are robust, with roughly constant scatter, if we select galaxies with $z_\text{phot} > 0.1$, for which the SMAD in $\Delta \log M_\star$ reduces to ~ 0.17 dex. Therefore we restrict the GGL analysis presented in the next section to this redshift range; the removed galaxies would not be of much importance for the lensing analysis in any case.

We used the absolute r-band magnitude and the rest-frame $u - g$ color derived with LePhare (employing the ANNz2 photo-zs as input redshifts) to select red and blue galaxies based on an empirical cut through the green valley in the color-magnitude diagram. We identified the ridge of the blue cloud to define the slope and locate the minimum at the absolute magnitude of $M_r = -19$. This results in a line that delimits the red and blue sample:

$$u - g = 0.825 - 0.025 M_r .\tag{2}$$

Based on this cut, we define our red sample as those galaxies whose $u - g$ color is at least 0.05 mag above the cut line and the blue sample as those whose color is at least 0.05 mag below the line. The color-magnitude distribution and the cut through the green valley are shown in Fig. 6. The photo-z statistics for the red and blue galaxies defined this way have been presented in Sect. 3; below in Sect. 5, we use this split as well as the stellar masses in GGL measurements.

5. Galaxy-galaxy lensing measurements

As shown in the previous section, the excellent photometric redshift estimates for the galaxies in the KiDS-Bright sample allow for robust estimates of their physical characteristics, in particular the stellar mass. In this section we combine this information with accurate shape measurements for more distant KiDS sources from Giblin et al. (2021) to measure the GGL signal. We first compared the lensing signal for a similar selection of lenses from GAMA and KiDS around the mode of the stellar mass distribution. We then split the sample of bright lens galaxies into blue and red subsamples (see Sect. 4 and Fig. 6), which were subsequently subdivided by stellar mass. To quantify the weak gravitational lensing signal, we used source galaxies from KiDS DR4 with a BPZ photo-z in the range $0.1 < z_B < 1.2$.

The lensing signal of an individual lens is too small to be detected, and hence we computed a weighted average of the tangential ellipticity ϵ_t as a function of projected distance r_p using a large number of lens-source pairs. In the weak lensing regime, this provides an unbiased estimate of the tangential shear, γ_t, which in turn can be related to the excess surface density (ESD) $\Delta\Sigma(r_p)$, defined as the difference between the mean projected surface mass density inside a projected radius r_p and the mean surface density at r_p.

We computed a weighted average to account for the variation in the precision of the shear estimate, captured by the *lens*fit weight w_s (see Fenech Conti et al. 2017; Kannawadi et al. 2019, for details), and the fact that the amplitude of the lensing signal depends on the source redshift. The weight assigned to each lens-source pair is

$$\widetilde{w}_\text{ls} = w_s \left(\widetilde{\Sigma}_\text{cr,ls}^{-1} \right)^2 ,\tag{3}$$

the product of the *lens*fit weight w_s and the square of $\widetilde{\Sigma}_\text{cr,ls}^{-1}$ – the effective inverse critical surface mass density, which is a geometric term that downweights lens-source pairs that are close in redshift (e.g., Bartelmann & Schneider 2001).

We computed the effective inverse critical surface mass density for each lens using the photo-z of the lens z_l and the full normalized redshift probability density of the sources, $n(z_s)$. The latter was calculated by employing the self-organizing map calibration method, originally presented in Wright et al. (2020), and then applied to KiDS DR4 in Hildebrandt et al. (2021). The resulting effective inverse critical surface density can be written as follows:

$$\widetilde{\Sigma}_\text{cr,ls}^{-1} = \frac{4\pi G}{c^2} \int_0^\infty (1 + z_l)^2 D(z_l) \left(\int_{z_l}^\infty \frac{D(z_l, z_s)}{D(z_s)} n(z_s)\, dz_s \right) p(z_l)\, dz_l ,\tag{4}$$

where $D(z_l)$, $D(z_s)$, and $D(z_l, z_s)$ are the angular diameter distances to the lens, source, and between the lens and the source, respectively.

For the lens redshifts z_l, we used the ANNz2 photo-zs of the KiDS-Bright foreground galaxy sample. We implemented the

contribution of z_l by integrating over the individual redshift probability distributions $p(z_l)$ of each lens. This method is shown to be accurate in Brouwer et al. (2021). The lensing kernel is wide and therefore the results are not sensitive to the small wings in the lens redshift probability distributions (see Sect. 3.2). We can thus safely assume that $p(z_l)$ can be described by a normal distribution centered at the lens's photo-z, with a standard deviation of $\sigma_z/(1 + z_l) = 0.018$ (see Sect. 3). This simplification over the better-fitted Lorentzian model (Eq. 1) does not induce significant biases in the present analysis as it will only lead to slightly underestimated errorbars of the lensing signal. In the future, as the statistical power of such measurements increases, these types of details might need to be taken into account, however.

For the source redshifts z_s, we followed the method used in Dvornik et al. (2018) by integrating over the part of the redshift probability distribution $n(z_s)$ where $z_s > z_l$. Thus, the ESD can be directly computed in bins of projected distance r_p to the lenses as follows:

$$\Delta\Sigma_{\mathrm{gm}}(r_{\mathrm{p}}) = \left[\frac{\sum_{\mathrm{ls}} \widetilde{w}_{\mathrm{ls}} \epsilon_{\mathrm{t,s}} \Sigma'_{\mathrm{cr,ls}}}{\sum_{\mathrm{ls}} \widetilde{w}_{\mathrm{ls}}} \right] \frac{1}{1+\overline{m}} , \qquad (5)$$

where $\Sigma'_{\mathrm{cr,ls}} \equiv 1/\widetilde{\Sigma}^{-1}_{\mathrm{cr,ls}}$, the sum is over all source-lens pairs in the distance bin, and

$$\overline{m} = \frac{\sum_i w'_i m_i}{\sum_i w'_i} \qquad (6)$$

is an average correction to the ESD profile that has to be applied to account for the multiplicative bias m in the *lens*fit shear estimates. The sum goes over thin redshift slices for which m was obtained using the method presented in Kannawadi et al. (2019), weighted by $w' = w_s \, D(z_l, z_s)/D(z_s)$ for a given lens-source sample. The value of $\overline{m}$ is around -0.014, independent of the scale at which it was computed.

We note that the measurements presented here are not corrected for the contamination of the source sample by galaxies that are physically associated with the lenses (the so-called boost correction). The impact on $\Delta\Sigma$ is minimal, however, as a result of the weighting with the inverse square of the critical surface density in Eqn. (4) (see for instance the bottom panel of fig. A4 in Dvornik et al. 2017). We also did not subtract the signal around random points, which suppresses large-scale systematics and sample variance (Singh et al. 2017; Dvornik et al. 2018). This improves the robustness of the measurements on scales above $2h^{-1}$ Mpc (Dvornik et al. 2018), which are not particularly relevant in constraining the halo model and halo occupation distribution parameters, and mostly affect the bias present in the 2-halo term, which we do not consider here (see Sect. 5.2).

5.1. Comparison with lenses from GAMA

As a first demonstration of the statistical power of the KiDS-Bright sample for GGL measurements, and to verify the quality of our photometrically selected lens sample, we directly compared the stacked excess surface density profile, $\Delta\Sigma$, with that of lenses extracted from GAMA. For the comparison, we used the stellar masses from the two respective surveys and defined a bin of 0.5 dex around the mode of the $\log M_\star$ distribution, which in both cases is ~ 10.75. This selection of $10.5 \leq \log(M_\star/M_\odot) \leq 11.0$ gives about 68 000 galaxies in GAMA and 352 000 in KiDS-Bright; in both cases, this is $\sim 35\%$ of the full sample. The resulting excess surface density $\Delta\Sigma$, multiplied by the projected distance from the lens r_p to enhance the large-scale signal, is presented in Fig. 7 as a function of r_p.
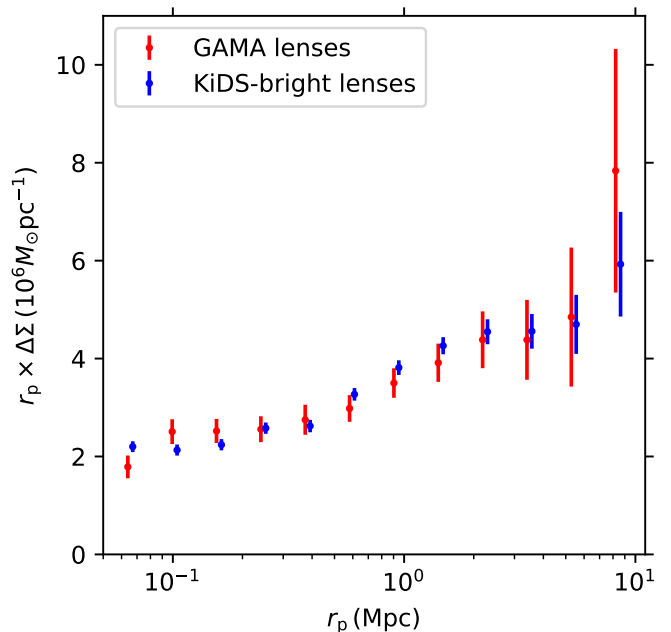

Fig. 7. Stacked excess surface density profiles, $\Delta\Sigma$ (multiplied by the distance from the lens r_p in megaparsecs), around lenses with $\log(M_\star/M_\odot) \in [10.5, 11.0]$. The red points show results for 68 000 lenses selected from GAMA, whereas the blue points show the signal around 352 000 lenses from the KiDS-Bright sample. The KiDS measurements were shifted slightly to the right for clarity.

The two measurements agree remarkably well, demonstrating that our photo-zs are sufficient for GGL studies. The small differences in the central values in Fig. 7 most likely arise from the inclusion of the whole KiDS-South area to the lensing study. The reduction in uncertainties also agrees with our expectation: for all scales, $\delta\Delta\Sigma_{\mathrm{GAMA}}/\delta\Delta\Sigma_{\mathrm{KiDS}} \approx 2.4$, which reflects the fact that the KiDS-Bright sample contains $\sim 5.6\times$ more galaxies. We also tested how much statistical power we lose by using photo-zs. For this we extracted the lensing signal in the same way as for GAMA, namely using the point estimate of the redshift, without its uncertainty (by dropping the integration over $p(z_l)$ in Eqn. 4). We found that the statistical power is worsened by only $\sim 5\%$ when propagating the redshift uncertainty through to the final lensing signal stack.

The precision improves slightly when the data for the full survey area (1350 deg^2) are included. This will make it possible to revisit the earlier study by Brouwer et al. (2018) of the lensing signal of "troughs" and "ridges" in the density field of KiDS galaxies, based on the much smaller catalog derived by B18. The sample we present in this paper has already been used in other analyses. Brouwer et al. (2021) selected isolated galaxies to measure the radial gravitational acceleration around them based on weak lensing measurements, thus extending the so-called radial acceleration relation into the low acceleration regime beyond the outskirts of the observable galaxies. The sample was also used by Johnston et al. (2021) as a test-bed for a new method to mitigate observational systematics in angular clustering measurements, in which self-organizing maps are taught the multivariate relationships between observed galaxy number density and systematic tracer variables. This was then used to create corrective random catalogs with spatially variable number densities, mimicking the systematic density modes in the data.
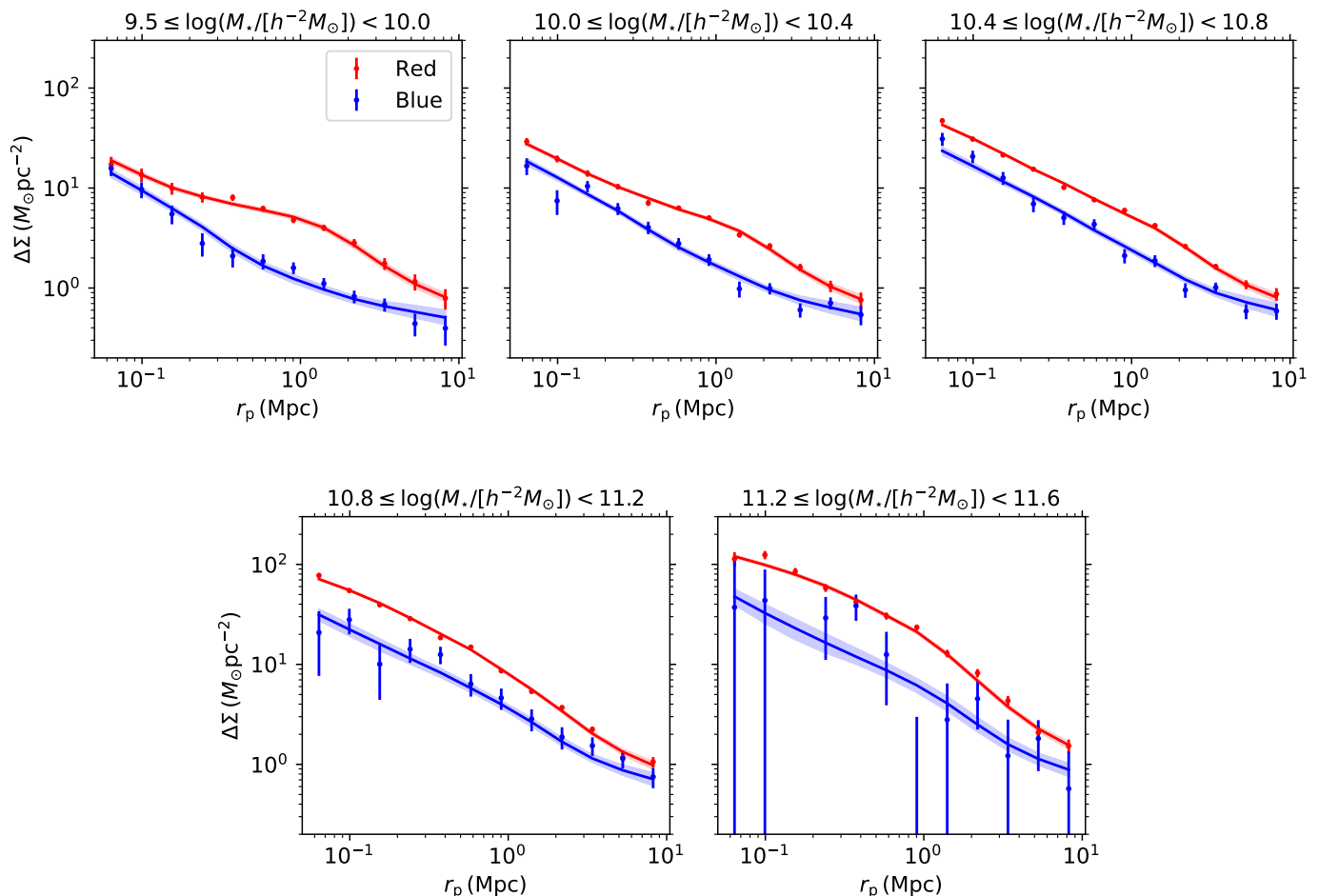
Fig. 8. Stacked excess surface density profiles, $\Delta\Sigma$, of the red and blue lenses (points in corresponding colors) in our KiDS-Bright sample in the four stellar mass bins labeled at the top. The lines indicate the best-fitting halo model, with contributions from both centrals and satellites (red and blue lines with shaded bands enclosing the 68% credible intervals). We note that the model was fit to all stellar mass bins simultaneously, but separately for the red and blue populations.

The improvement in statistical power will also allow for better constraints on the halo model and the associated halo occupation properties. The small-scale measurements accessible with such a sample will provide better constraints on the galaxy bias in the nonlinear regime and allow us to test our assumption about the validity of the halo model. Finally, we anticipate that this kind of wide-angle lens sample can improve cosmological constraints from multi-probe analyses employing GGL.

5.2. Stellar-to-halo-mass relation

As a further demonstration of the quality of our data, we used the KiDS-Bright sample to explore the stellar-to-halo-mass relation (SHMR) for the blue and red galaxies separately. Earlier GGL studies have shown that these differ (e.g., Hoekstra et al. 2005; Velander et al. 2014; Mandelbaum et al. 2016), which is also seen in hydrodynamic simulations (e.g., Correa & Schaye 2020). Nonetheless there is no consensus in the literature yet because other approaches have arrived at different conclusions (see Wechsler & Tinker 2018, for a detailed overview and discussion). Some of the differences may arise from the stellar mass estimates and the specific selection of the subsamples. For this reason we do not compare our findings to the literature, but defer such a detailed comparison to future work. Our aim is merely to demonstrate the potential of our data for studies of the SHMR.

We split the KiDS-Bright sample by color using the cut defined in Sect. 4 (see Fig. 6). We selected lenses with $z_{phot} > 0.1$ and used our stellar mass estimates to subdivide the blue and red galaxies into five stellar mass intervals, with the bin edges: $\log\left(M_\star/[h^{-2}M_\odot]\right) = \{9.5, 10.0, 10.4, 10.8, 11.2, 11.6\}$. In this section we give results in terms of an explicitly h-dependent mass unit, as used in our modeling, rather than adopting the specific value $h = 0.7$, as used elsewhere. The properties of the subsamples are reported in Table 2. For each stellar mass bin of the two color selections, we measured the lensing signal as described above, and the results are shown in Fig. 8. For all subsamples we detect a significant signal, demonstrating the value of our bright galaxy selection.

To infer the corresponding halo masses, we need to fit a model to the lensing signal. Numerical simulations show that the dark matter distribution in halos is well described by an Navarro-Frenk-White (NFW) profile (Navarro et al. 1997), but the signals shown in Fig. 8, especially those of the red galaxies with low stellar masses, show a more complex dependence with radius. At large radii the lensing signal is enhanced by the clustering of galaxies, whereas on small scales satellite galaxies contribute, causing a wide "bump" around 1 Mpc.

The influence of neighboring galaxies can be reduced by selecting "isolated" lenses, so that a simple model can still describe the measurements. This approach was used by Hoekstra et al.

Table 2. Overview of the number of lens galaxies, median stellar masses of the galaxies, and median redshifts in each selected mass bin.

Bin	$\log M_\star$ range	$N_{\rm red}$	$\log M_{\star,{\rm med}}^{({\rm red})}$	$z_{\rm med}^{({\rm red})}$
1	[9.5,10.0)	52 813	9.83	0.16
2	[10.0,10.4)	119 038	10.23	0.23
3	[10.4,10.8)	147 342	10.58	0.29
4	[10.8,11.2)	52 320	10.92	0.36
5	[11.2,11.6)	4 342	11.28	0.43
Bin	$\log M_\star$ range	$N_{\rm blue}$	$\log M_{\star,{\rm med}}^{({\rm blue})}$	$z_{\rm med}^{({\rm blue})}$
1	[9.5,10.0)	97 786	9.75	0.22
2	[10.0,10.4)	85 594	10.20	0.29
3	[10.4,10.8)	60 541	10.55	0.36
4	[10.8,11.2)	8 839	10.88	0.40
5	[11.2,11.6)	428	11.31	0.41

Notes. Stellar masses are given in units of $\log\left(M_\star/[h^{-2}M_\odot]\right)$. The median stellar masses are used as an estimate of the stellar contribution to the total lensing signal described as a point-like source.

Table 3. Parameter space ranges and marginalized posterior estimates of the free parameters used in our model, for both the red and blue sample.

Parameter	Priors	Red	Blue
f_c	[0, 1]	$0.993^{+0.002}_{-0.021}$	–
$\log(M_0/[h^{-2}M_\odot])$	[7, 13]	$10.39^{+0.14}_{-0.15}$	$10.11^{+0.980}_{-0.087}$
$\log(M_1/[h^{-2}M_\odot])$	[9, 14]	$11.74^{+0.18}_{-0.20}$	$11.78^{+0.59}_{-0.38}$
γ_1	$\mathcal{N}(3, 3)$	$5.0^{+2.2}_{-1.6}$	$2.1^{+1.0}_{-1.0}$
γ_2	[0, 10]	$0.47^{+0.17}_{-0.14}$	$0.65^{+0.56}_{-0.50}$
σ_c	[0.05, 2.5]	$0.064^{+0.046}_{-0.014}$	$0.28^{+0.36}_{-0.18}$
b	[0.2, 5]	$0.90^{+0.15}_{-0.11}$	$0.73^{+0.26}_{-0.25}$
f_s	[0, 1]	$0.56^{+0.29}_{-0.15}$	–
α_s	$\mathcal{N}(-1.1, 0.9)$	$-1.286^{+0.121}_{-0.079}$	$-0.75^{+0.23}_{-0.14}$
b_1	$\mathcal{N}(0.0, 1.5)$	$-0.65^{+0.12}_{-0.14}$	$-0.42^{+0.41}_{-0.22}$
b_2	$\mathcal{N}(1.5, 1.5)$	$0.97^{+0.18}_{-0.13}$	$0.63^{+0.81}_{-0.61}$

Notes. M_0 is the normalization of the stellar-to-halo mass relation (SHMR); M_1 is the characteristic mass scale of the same SHMR; f_c is the normalization of the concentration-mass relation; σ_c is the scatter between the stellar and halo mass; γ_1 and γ_2 are the low and high-mass slopes of the SHMR; f_s is the normalization of the concentration–mass relation for satellite galaxies; and α_s, b_0, and b_1 govern the behavior of the satellite galaxies. As the parameters f_c and f_s of the blue sample are not constrained and they recover the prior ranges, we do not provide their values. As discussed in the text, the parameters that describe the CSMF are biased as a result of the cut in apparent magnitude that defines the KiDS-Bright sample.

(2005) and Brouwer et al. (2021), but at the expense of significantly reducing the lens sample size. Here, inspired by the halo model (Seljak 2000; Cooray & Sheth 2002), we estimate the mean halo mass of central galaxies as a function of stellar mass by modeling the contributions of both central and satellite galaxies jointly. The SHMR of central galaxies is parameterized using the following equation:

$$M_\star(M_{\rm h}) = M_0 \frac{(M_{\rm h}/M_1)^{\gamma_1}}{[1 + (M_{\rm h}/M_1)]^{\gamma_1 - \gamma_2}} . \tag{7}$$

This relation has an intrinsic scatter, and we assume that the distribution of $\log(M_\star)$ at a fixed halo mass is a Gaussian with a dispersion σ_c. It is important to include this intrinsic scatter as it enables the model to account for Eddington bias (Leauthaud et al. 2012; Cacciato et al. 2013).

The model itself is based on the halo model implementation presented in van Uitert et al. (2016), but in our case we adopted a separate normalization of the concentration of the dark matter density profile for central and satellite galaxies, a free normalization of the two-halo term, and a fixed subhalo mass for satellite galaxies. The free parameters that describe the lensing signal around a galaxy with a given mass are thus the following: the normalization of the concentration-mass relation for central galaxies, f_c; the normalization of the SHMR, M_0; its characteristic mass scale, M_1; the low and high mass end slopes, γ_1 and γ_2; and the normalization of the concentration-mass relation for satellite galaxies, f_s. We simply fit for the normalization of the 2-halo term, b, but did not aim to interpret its value.

The number density of halos of a given stellar mass is not uniform, and this needs to be accounted for in the model. Moreover, in doing so, we need to distinguish between central and satellite galaxies because the satellite fraction itself depends on mass. To do so, we used the conditional stellar mass function (CSMF), which we describe in more detail in Appendix B. This introduces the following additional parameters: the high mass slope of the Schechter function, α_s, and the free parameters for the normalization of the Schechter function used for satellite galaxies, b_1 and b_2. Finally, we note that we assume that none of the parameters depend on redshift and that the parameters of the Schechter function are constrained by the lensing signal alone.

The model, as detailed in Appendix B, implicitly assumes that we employed a complete volume-limited sample of lenses.

This is not the case here because the cut in apparent r-band magnitude leads to incompleteness that is larger for low stellar masses, with the selection of red galaxies affected the most. A proper analysis, which is beyond the scope of our exploratory study, would have to explicitly include the apparent magnitude cut of the sample in the model. This is also required if one would like to jointly model the GGL signal, the stellar mass function, and the clustering signal.

The observed lensing signal is, however, most sensitive to the average halo mass of the sample of lenses, so that the resulting mean SHMR for central galaxies is expected to be close to the true one. We stress, however, that the parameters that describe the CSMF will be biased. To test this expectation, we examined how the magnitude cut changes the stellar mass and halo mass distributions. We used the MICEv2 simulations[8] (Carretero et al. 2015; Crocce et al. 2015; Fosalba et al. 2015b,a) to select central galaxies with $0.1 < z < 0.5$, which we split into blue and red samples. We used the definitions of stellar mass bins listed in Table 2 and computed the corresponding mean stellar and halo masses. We also repeated the measurements, after we applied a cut in apparent magnitude, $m_r < 20$, to mimic the selection of the KiDS-Bright sample. As expected, the resulting stellar mass functions are biased low for low stellar masses, with the red galaxies being affected the most. In contrast, the changes in the mean SHMR are small: the mean $\log(M_\star)$ is less than 0.05 dex lower and the intrinsic scatter is not significantly affected either. Given the uncertainties in the stellar masses themselves, we therefore conclude that the magnitude cut has a negligible im-
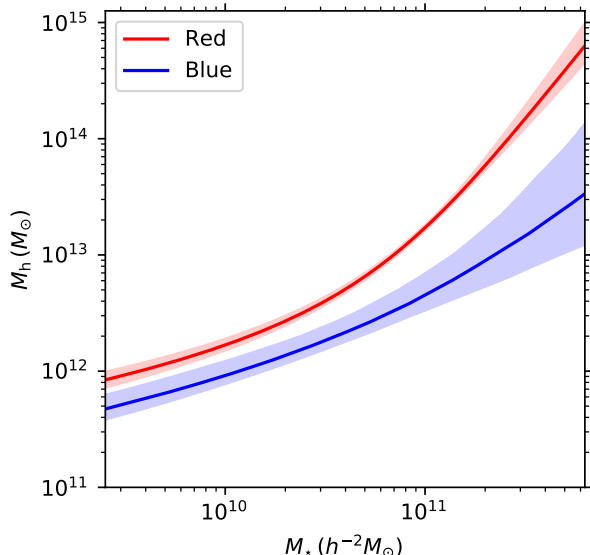
---

[8] http://maia.ice.cat/mice/

Fig. 9. Predicted halo mass as a function of the stellar mass for red and blue galaxies from this study, using the halo model parameters listed in Table 3.

pact on the inferred SHMR. Nonetheless, we defer a quantitative interpretation of the results to future work.

We fit our model (see Appendix B for a summary) to the lensing signal of each of the color-selected subsamples (that is, a single model for all the stellar mass bins). The priors that we used are listed in Table 3. Most priors are flat in the given ranges; the instances with a Gaussian prior are indicated as $\mathcal{N}(\bar{x}, \sigma(x))$, with mean $\bar{x}$ and a standard deviation $\sigma(x)$. In the fit we used the bootstrap covariance matrix measured directly on the data (for details see Viola et al. 2015; Dvornik et al. 2018), with the correction from Hartlap et al. (2007) applied to account for noise in the covariance matrix.

The best-fit parameters obtained with the Markov chain Monte Carlo method (Foreman-Mackey et al. 2013) for the halo model are reported in Table 3, and we show the corresponding models in Fig. 8 as lines, with shaded areas indicating the uncertainty. The reduced $\chi^2_{\rm red}$ of the halo model fit is 1.92 and 1.91 for the red and blue samples, respectively, with 48 degrees of freedom. Although the $\chi^2_{\rm red}$ values are high, we note that our model is only an effective description of the signal; our small statistical uncertainties may already point to the need to improve the modeling itself (e.g., Mead & Verde 2021; Sugiyama et al. 2020). The best-fit SHMR models and their uncertainties for the red and blue samples are shown in Fig. 9. The data cannot constrain the concentration normalization of blue central and satellite galaxies, and for these parameters we recover their prior ranges.

Our lensing results suggest that red galaxies with observed stellar masses of $M_\star < 5 \times 10^{10} h^{-2} M_\odot$ occupy dark matter halos that are about a factor of two more massive than those of blue galaxies with similar stellar masses. At the high mass end, however, the differences are larger and red galaxies at a given stellar mass are found in much more massive halos. Qualitatively, these results are in good agreement with the bimodality found by Mandelbaum et al. (2016).

The accuracy of the stellar mass estimates from SED modeling suffer from systematic uncertainties, arising from assumptions about the star formation history, the initial mass function, or the photometry itself. Although our split by rest-frame color might exacerbate such systematics, the difference we observe is

too large to be solely attributed to them. Nonetheless, a more detailed investigation is needed before we can quantify the various sources of bias more reliably. Moreover, as discussed above, our model does not fully capture the impact of the magnitude limit of the KiDS-Bright sample. Similarly, a quantitative comparison with previous results (e.g., Velander et al. 2014; Mandelbaum et al. 2016) requires a careful replication of their sample selections and stellar mass determination.

6. Conclusions and future prospects

We selected a sample of bright galaxies using the 9-band photometry from KiDS DR4 (Kuijken et al. 2019) that closely resembles the highly complete spectroscopic dataset from GAMA (Driver et al. 2011). For an optimal completeness-purity trade-off, we applied a KiDS magnitude limit of $r_{\rm auto} < 20$ and employed three star-galaxy separation criteria based on KiDS photometry. This resulted in a highly pure sample of galaxies that matches the properties of GAMA very well, with only $\sim 1\%$ of the KiDS-Bright galaxies not represented with respect to GAMA. The dataset probes the large-scale structure at a mean redshift of $\langle z \rangle \simeq 0.23$ and reaches up to $z \lesssim 0.5$, although with decreasing completeness at these high redshifts due to its flux-limited character.

The very good match between the two samples allowed us to take full advantage of supervised machine learning regression and derive statistically accurate and precise photometric redshifts for the entire KiDS-Bright catalog. To do so, we used artificial neural networks implemented in the ANNz2 package (Sadeh et al. 2016). The resulting photo-zs have a small scatter of $\sigma_z \sim 0.018(1 + z)$ and a mean bias $|\langle \delta z \rangle| < 10^{-3}$. The photo-$z$ performance does not depend on the r-band magnitude nor on the photo-z for $0.05 < z_{\rm phot} < 0.5$. The photo-$z$ error distribution is close to Gaussian, but a generalized Lorentzian captures the slightly broader wings better.

We exploited the nine-band coverage and the high-quality photo-zs to derive robust absolute magnitudes, rest-frame colors, and stellar masses using the LePhare SED-fitting tool (Arnouts et al. 1999). We employed these derivations to split the sample into red and blue galaxies based on the rest-frame $u - g$ color and absolute r-band magnitude. The red galaxies have better photo-zs than the full sample, with $\sigma_z \sim 0.015(1 + z)$ at the mean redshift $\langle z \rangle \sim 0.27$. Nonetheless, the photo-zs for the blue galaxies are also excellent with $|\langle \delta z \rangle| \sim 10^{-3}$ and $\sigma_z \sim 0.019(1 + z)$). This exquisite performance is achieved thanks to the very complete coverage of the GAMA training set, which is free of any color preselections.

A comparison of the stellar masses with independent estimates from GAMA (Taylor et al. 2011; Wright et al. 2016) shows excellent agreement, with $\Delta \log M_\star \equiv \log M_\star^{\rm KiDS} - \log M_\star^{\rm GAMA} = -0.09 \pm 0.18$ dex (median and SMAD). Our use of photometric redshifts accounts for 9% of this scatter, demonstrating the sample's potential for scientific exploitation. As a scientific verification of the KiDS-Bright dataset, we measured the galaxy-galaxy lensing signal for galaxies with stellar masses in the range $10.5 \le \log M_\star/M_\odot \le 11$ and compared these directly to a similar selection using GAMA only. The lensing signals agree over two decades in angular separation, while the uncertainties are a factor of ~ 2.4 smaller for the sample of KiDS-Bright lenses.

Motivated by this agreement, we measured the lensing signal around the blue and red galaxies in five stellar mass bins, ranging from $\log \left(M_\star/h^{-2} M_\odot \right) = 9.5$ to 11.6, and we detected significant signals in all cases. The measurements were fitted with

a model that includes both central and satellite galaxies (e.g., Dvornik et al. 2018). Their relative contributions as a function of stellar mass are described using a conditional stellar mass function. The resulting parameters, however, are biased, because the KiDS-Bright magnitude limit leads to incompleteness at low stellar masses, with the red sample being affected the most. Fortunately, a comparison to a simulated catalog of galaxies from MICEv2 suggests that the SHMR is not affected significantly.

We used this model to constrain the SHMR for blue and red galaxies separately. We find that blue and red galaxies with observed stellar masses of $M_\star < 5 \times 10^{10} h^{-2} M_\odot$ occupy dark matter halos that are about a factor two more massive than those of blue galaxies with similar stellar masses. For stellar masses of $M_\star \gtrsim 10^{11} h^{-2} M_\odot$, the model predicts however that the dark matter halos of red galaxies are much more massive than those of blue galaxies with the same stellar mass. This result is in good qualitative agreement with similar findings by Mandelbaum et al. (2016). A more detailed comparison, however, is beyond the scope of this paper because it would also require a careful comparison of the stellar masses, whilst accounting for differences in the sample selection.

Our results demonstrate the value of combining highly complete spectroscopy with high-quality imaging data. In the coming decade, further advances will be made on both fronts. Large spectroscopic surveys will probe both larger volumes and fainter galaxies than current wide-angle redshift catalogs, to the benefit of the already existing imaging surveys. In the case of KiDS, further improvements will be possible thanks to new overlapping complete redshift samples deeper than GAMA, such as the ongoing Deep Extragalactic VIsible Legacy Survey (DEVILS, Davies et al. 2018) that aims at a very complete selection with a flux limit of $Y < 21.2$ in fields that partly overlap with KiDS imaging. On a longer timescale, the 4-metre Multi-Object Spectroscopic Telescope (4MOST, de Jong et al. 2019) should deliver denser redshift coverage than GAMA over the full KiDS area, in particular from its Wide-Area VISTA Extragalactic (WAVES, Driver et al. 2019) and Cosmology Redshift Surveys (Richard et al. 2019).

Such larger and deeper spectroscopic data will be ideally suited to exploit Stage-IV imaging surveys, such as the Rubin Observatory's Legacy Survey of Space and Time (LSST Science Collaboration et al. 2009) and *Euclid* (Laureijs et al. 2011). Those will cover areas more than 10× larger at a greater depth than the Stage-III surveys such as KiDS. The resulting increase in the statistical power will, however, require much better handling of systematics, starting from those in the selection of lenses for GGL and 3×2pt analyses. Our study demonstrates that one possible approach toward this goal is to extract a well-characterized, flux-limited galaxy catalog, provided that a matched spectroscopic subsample is available to calibrate this selection and to estimate robust photometric redshifts. Such samples can be enhanced with deeper, yet less complete, photometric selections of luminous red galaxies (e.g., Rozo et al. 2016; Vakili et al. 2020) and adaptive magnitude cuts as a function of photo-z (Porredon et al. 2021) to probe a larger range of lens redshifts and luminosities.

References

Abazajian K. N., et al., 2009, ApJS, 182, 543
Abbott T. M. C., et al., 2018, Phys. Rev. D, 98, 043526
Abolfathi B., et al., 2018, ApJS, 235, 42
Aihara H., et al., 2018, PASJ, 70, S4
Alam S., et al., 2017, MNRAS, 470, 2617
Alam S., et al., 2021, Phys. Rev. D, 103, 083533
Alarcon A., et al., 2021, MNRAS, 501, 6103
Amon A., et al., 2018, MNRAS, 479, 3422
Arnouts S., Cristiani S., Moscardini L., Matarrese S., Lucchin F., Fontana A., Giallongo E., 1999, MNRAS, 310, 540
Balaguera-Antolínez A., Bilicki M., Branchini E., Postiglione A., 2018, MNRAS, 476, 1050
Baldry I. K., et al., 2010, MNRAS, 404, 86
Baldry I. K., et al., 2012, MNRAS, 421, 621
Baldry I. K., et al., 2018, MNRAS, 474, 3875
Baldry I. K., Sullivan T., Rani R., Turner S., 2021, MNRAS, 500, 1557
Bartelmann M., Schneider P., 2001, Phys. Rep., 340, 291
Beck R., Szapudi I., Flewelling H., Holmberg C., Magnier E., Chambers K. C., 2021, MNRAS, 500, 1633
Bellstedt S., et al., 2020, MNRAS, 496, 3235
Benítez N., 2000, ApJ, 536, 571
Bertin E., Arnouts S., 1996, A&AS, 117, 393
Bilicki M., Jarrett T. H., Peacock J. A., Cluver M. E., Steward L., 2014, ApJS, 210, 9
Bilicki M., et al., 2018, A&A, 616, A69
Blake C., et al., 2016, MNRAS, 462, 4240
Blake C., et al., 2020, A&A, 642, A158
Brouwer M. M., et al., 2016, MNRAS, 462, 4451
Brouwer M. M., et al., 2017, MNRAS, 466, 2547
Brouwer M. M., et al., 2018, MNRAS, 481, 5189
Brouwer M. M., et al., 2021, A&A, 650, A113
Bruzual G., Charlot S., 2003, MNRAS, 344, 1000

Cacciato M., van den Bosch F. C., More S., Mo H., Yang X., 2013, MNRAS, 430, 767

Calzetti D., Kinney A. L., Storchi-Bergmann T., 1994, ApJ, 429, 582

Capaccioli M., et al., 2012, in Science from the Next Generation Imaging and Spectroscopic Surveys. p. 1

Carretero J., Castander F. J., Gaztañaga E., Crocce M., Fosalba P., 2015, MNRAS, 447, 646

Chabrier G., 2003, PASP, 115, 763

Cole S., et al., 2005, MNRAS, 362, 505

Cooray A., Sheth R., 2002, Phys. Rep., 372, 1

Correa C. A., Schaye J., 2020, MNRAS, 499, 3578

Coupon J., et al., 2015, MNRAS, 449, 1352

Crocce M., Castander F. J., Gaztañaga E., Fosalba P., Carretero J., 2015, MNRAS, 453, 1513

Dalton G. B., et al., 2006, in McLean I. S., Iye M., eds, Society of Photo-Optical Instrumentation Engineers (SPIE) Conference Series Vol. 6269, Society of Photo-Optical Instrumentation Engineers (SPIE) Conference Series. p. 62690X, doi:10.1117/12.670018

Davies L. J. M., et al., 2018, MNRAS, 480, 768

Dawson K. S., et al., 2013, AJ, 145, 10

Driver S. P., et al., 2011, MNRAS, 413, 971

Driver S. P., et al., 2016, MNRAS, 455, 3911

Driver S. P., et al., 2019, The Messenger, 175, 46

Dvornik A., et al., 2017, MNRAS, 468, 3251

Dvornik A., et al., 2018, MNRAS, 479, 1240

Eardley E., et al., 2015, MNRAS, 448, 3665

Edge A., Sutherland W., Kuijken K., Driver S., McMahon R., Eales S., Emerson J. P., 2013, The Messenger, 154, 32

Emerson J., McPherson A., Sutherland W., 2006, The Messenger, 126, 41

Erben T., et al., 2005, Astronomische Nachrichten, 326, 432

Fenech Conti I., Herbonnet R., Hoekstra H., Merten J., Miller L., Viola M., 2017, MNRAS, 467, 1627

Foreman-Mackey D., Hogg D. W., Lang D., Goodman J., 2013, PASP, 125, 306

Fosalba P., Gaztañaga E., Castander F. J., Crocce M., 2015a, MNRAS, 447, 1319

Fosalba P., Crocce M., Gaztañaga E., Castander F. J., 2015b, MNRAS, 448, 2987

Gaia Collaboration et al., 2018, A&A, 616, A1

Giblin B., et al., 2021, A&A, 645, A105

Gunawardhana M. L. P., et al., 2011, MNRAS, 415, 1647

Hang Q., Alam S., Peacock J. A., Cai Y.-C., 2021, MNRAS, 501, 1481

Hartlap J., Simon P., Schneider P., 2007, A&A, 464, 399

Heymans C., et al., 2021, A&A, 646, A140

Hildebrandt H., et al., 2021, A&A, 647, A124

Hoekstra H., van Waerbeke L., Gladders M. D., Mellier Y., Yee H. K. C., 2002, ApJ, 577, 604

Hoekstra H., Hsieh B. C., Yee H. K. C., Lin H., Gladders M. D., 2005, ApJ, 635, 73

Hunter J. D., 2007, Computing in Science Engineering, 9, 90

Ilbert O., et al., 2006, A&A, 457, 841

Johnston H., et al., 2021, A&A, 648, A98

Jones D. H., et al., 2009, MNRAS, 399, 683

Jones E., Oliphant T., Peterson P., et al., 2001–, SciPy: Open source scientific tools for Python, http://www.scipy.org/

Joudaki S., et al., 2018, MNRAS, 474, 4894

Kannawadi A., et al., 2019, A&A, 624, A92

Kuijken K., 2008, A&A, 482, 1053

Kuijken K., 2011, The Messenger, 146, 8

Kuijken K., et al., 2015, MNRAS, 454, 3500

Kuijken K., et al., 2019, A&A, 625, A2

LSST Science Collaboration et al., 2009, preprint, (arXiv:0912.0201)

Laureijs R., et al., 2011, preprint, (arXiv:1110.3193)

Lawrence A., et al., 2007, MNRAS, 379, 1599

Leauthaud A., et al., 2012, ApJ, 744, 159

Linke L., et al., 2020, A&A, 640, A59

Liske J., et al., 2015, MNRAS, 452, 2087

Mandelbaum R., Wang W., Zu Y., White S., Henriques B., More S., 2016, MNRAS, 457, 3200

McFarland J. P., Verdoes-Kleijn G., Sikkema G., Helmich E. M., Boxhoorn D. R., Valentijn E. A., 2013, Experimental Astronomy, 35, 45

Mead A. J., Verde L., 2021, MNRAS, 503, 3095

Miller L., et al., 2013, MNRAS, 429, 2858

Nakoneczny S. J., et al., 2021, A&A, 649, A81

Navarro J. F., Frenk C. S., White S. D. M., 1997, ApJ, 490, 493

Pasquet J., Bertin E., Treyer M., Arnouts S., Fouchez D., 2019, A&A, 621, A26

Peacock J. A., Bilicki M., 2018, MNRAS, 481, 1133

Percival W. J., et al., 2001, MNRAS, 327, 1297

Petrosian V., 1976, ApJ, 210, L53

Porredon A., et al., 2021, Phys. Rev. D, 103, 043503

Richard J., et al., 2019, The Messenger, 175, 50

Robotham A. S. G., et al., 2011, MNRAS, 416, 2640

Rozo E., et al., 2016, MNRAS, 461, 1431

Sadeh I., Abdalla F. B., Lahav O., 2016, PASP, 128, 104502

Schlafly E. F., Finkbeiner D. P., 2011, ApJ, 737, 103

Schlegel D. J., Finkbeiner D. P., Davis M., 1998, ApJ, 500, 525

Seljak U., 2000, MNRAS, 318, 203

Sifón C., et al., 2015, MNRAS, 454, 3938

Singh S., Mandelbaum R., Seljak U., Slosar A., Vazquez Gonzalez J., 2017, MNRAS, 471, 3827

Soo J. Y. H., et al., 2018, MNRAS, 475, 3613

Strauss M. A., et al., 2002, AJ, 124, 1810

Sugiyama S., Takada M., Kobayashi Y., Miyatake H., Shirasaki M., Nishimichi T., Park Y., 2020, Phys. Rev. D, 102, 083520

Taylor M. B., 2005, in Shopbell P., Britton M., Ebert R., eds, Astronomical Society of the Pacific Conference Series Vol. 347, Astronomical Data Analysis Software and Systems XIV. p. 29

Taylor M. B., 2006, in Gabriel C., Arviset C., Ponz D., Enrique S., eds, Astronomical Society of the Pacific Conference Series Vol. 351, Astronomical Data Analysis Software and Systems XV. p. 666

Taylor E. N., et al., 2011, MNRAS, 418, 1587

The Dark Energy Survey Collaboration 2005, preprint, (arXiv:astro-ph/0510346)

Tian L., Hoekstra H., Zhao H., 2009, MNRAS, 393, 885

Tinker J. L., Robertson B. E., Kravtsov A. V., Klypin A., Warren M. S., Yepes G., Gottlöber S., 2010, Astrophys. J., 724, 878

Tröster T., et al., 2021, A&A, 649, A88

Vakili M., et al., 2019, MNRAS, 487, 3715

Vakili M., et al., 2020, preprint, (arXiv:2008.13154)

Velander M., et al., 2014, MNRAS, 437, 2111

Viola M., et al., 2015, MNRAS, 452, 3529

Wechsler R. H., Tinker J. L., 2018, ARA&A, 56, 435

Wolf C., et al., 2017, MNRAS, 466, 1582

Wright A. H., 2016, LAMBDAR: Lambda Adaptive Multi-Band Deblending Algorithm in R, Astrophysics Source Code Library (ascl:1604.003)

Wright A. H., et al., 2016, MNRAS, 460, 765

Wright A. H., et al., 2019, A&A, 632, A34

Wright A. H., Hildebrandt H., van den Busch J. L., Heymans C., Joachimi B., Kannawadi A., Kuijken K., 2020, A&A, 640, L14

Yang X., Mo H. J., van den Bosch F. C., 2008, Astrophys. J., 676, 248

de Jong J. T. A., Verdoes Kleijn G. A., Kuijken K. H., Valentijn E. A., 2013, Experimental Astronomy, 35, 25

de Jong J. T. A., et al., 2015, A&A, 582, A62

de Jong J. T. A., et al., 2017, A&A, 604, A134

de Jong R. S., et al., 2019, The Messenger, 175, 3

van Uitert E., et al., 2016, MNRAS, 459, 3251

van Uitert E., et al., 2017, MNRAS, 467, 4131

van Uitert E., et al., 2018, MNRAS, 476, 4662

van den Busch J. L., et al., 2020, A&A, 642, A200

van der Walt S., Colbert S. C., Varoquaux G., 2011, Computing in Science Engineering, 13, 22
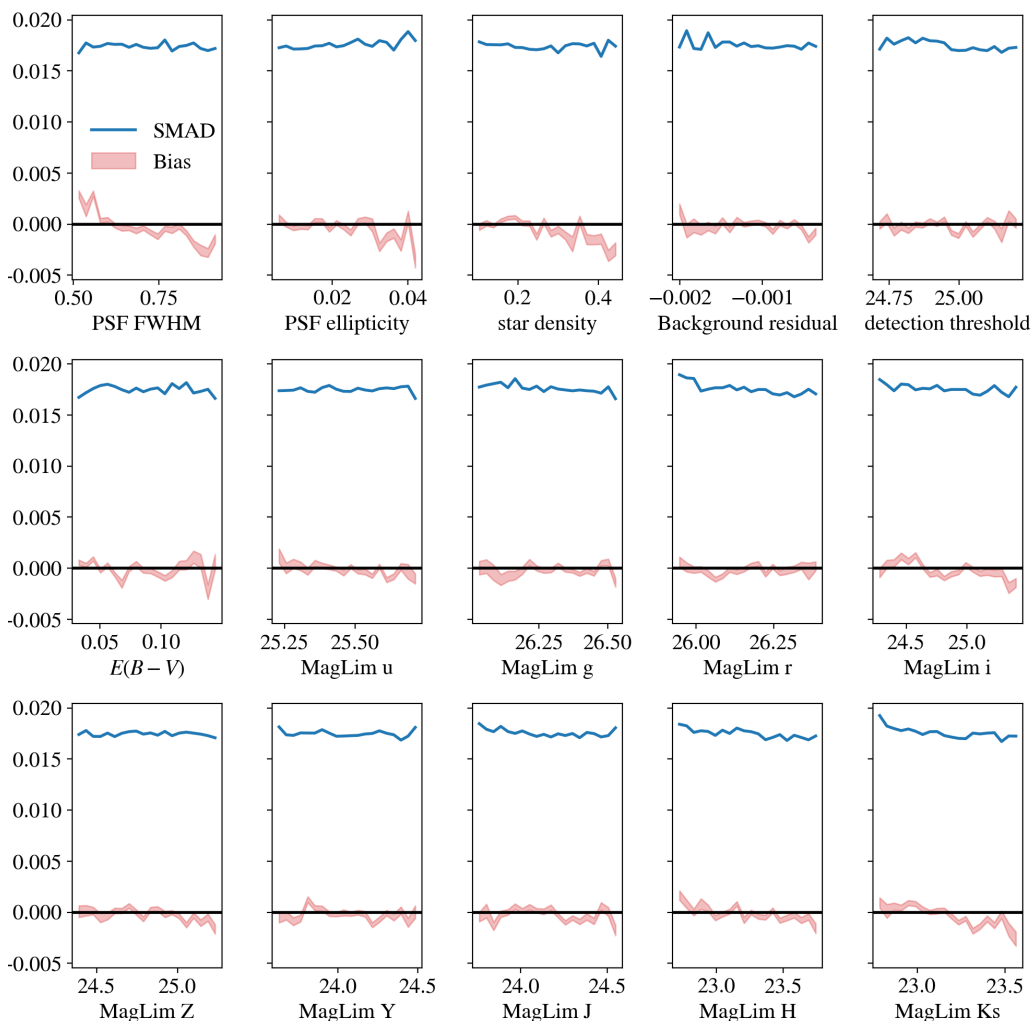
Fig. A.1. Photometric redshift quality (bias and scatter) as a function of KiDS-internal and external observational properties.

Appendix A: Dependence of photometric redshift quality on survey systematics

Here we present how the photo-zs of the KiDS-Bright sample described in Sect. 3 vary as a function of survey-related effects. In Figure A.1 we show the photo-z bias and scatter (SMAD) evaluated for a range of the following parameters:

- **PSF FWHM** (full width at half maximum) in the r-band, in units of arcseconds, calculated using the `PSF_Strehl_ratio` column in the catalog;
- **PSF ellipticity** in the r-band, obtained from the `PSFe1` and `PSFe2` columns;
- **Star density** (projected), determined from the pixelated number density map of bright stars in the second Gaia data release (Gaia Collaboration et al. 2018);
- **Background residual** counts in the centroid positions of the objects in the THELI-processed r-band detection images, provided as `BACKGROUND` in the catalog;
- **Detection threshold** above background in units of counts, provided as `THRESHOLD`;
- **E(B-V)**, Galactic dust extinction in the r-band, derived from the Schlegel et al. (1998) maps with the Schlafly & Finkbeiner (2011) corrections, provided as `EXTINCTION_r` in the catalog; and
- **MagLim**, limiting magnitudes in the 9 KV bands, evaluated at object position.

For more details on these quantities, please see Vakili et al. (2020).

Appendix B: Halo model

We modeled the halo occupation statistics using the conditional stellar mass function (CSMF, as also presented by Yang et al. 2008; Cacciato et al. 2013; van Uitert et al. 2016), and we employed them to calculate the $\mathcal{H}$ functions used in the halo model (Cacciato et al. 2013; van Uitert et al. 2016; Dvornik et al. 2018). The CSMF, $\Phi(M_\star|M_{\rm h})$, specifies the average number of galaxies of stellar mass $M_\star$ that reside in a halo of mass $M_{\rm h}$. In this formalism, the halo occupation statistics of central galaxies are defined via the following function:

$$\Phi(M_\star|M_{\rm h}) = \Phi_{\rm c}(M_\star|M_{\rm h}) + \Phi_{\rm s}(M_\star|M_{\rm h}) .$$
(B.1)

In particular, the CSMF of central galaxies was modeled as a log-normal,

$$\Phi_c(M_\star|M_h) = \frac{1}{\sqrt{2\pi}\ln(10)\,\sigma_c M_\star}\exp\left[-\frac{\log(M_\star/M_c^*)^2}{2\,\sigma_c^2}\right],$$

(B.2)

and the satellite term as a modified Schechter function,

$$\Phi_s(M_\star|M_h) = \frac{\phi_s^*}{M_s^*}\left(\frac{M_\star}{M_s^*}\right)^{\alpha_s}\exp\left[-\left(\frac{M_\star}{M_s^*}\right)^2\right],$$

(B.3)

where σ_c is the scatter between stellar mass and halo mass and α_s governs the power law behavior of satellite galaxies. We note that M_c^*, σ_c, ϕ_s^*, α_s, and M_s^* are, in principle, all functions of halo mass M_h. We assume that σ_c and α_s are independent of the halo mass M_h. Halo masses are drawn from the halo mass function for which we assume the Tinker et al. (2010) fitting function. Inspired by Yang et al. (2008), we parameterize M_c^*, M_s^*, and ϕ_s^* as:

$$M_c^*(M_h) = M_0\frac{(M_h/M_1)^{\gamma_1}}{[1+(M_h/M_1)]^{\gamma_1-\gamma_2}},$$

(B.4)

$$M_s^*(M_h) = 0.56\,M_c^*(M_h),$$

(B.5)

and

$$\log[\phi_s^*(M_h)] = b_0 + b_1(\log m_{13}),$$

(B.6)

where $m_{13} = M_h/(10^{13}M_\odot)$. The factor of 0.56 is also inspired by Yang et al. (2008) and further tests by van Uitert et al. (2016) have shown that using this assumption does not significantly affect the results.

From the CSMF, it is straightforward to compute the halo occupation numbers. The average number of galaxies with stellar masses in the range from $M_{\star,1} \leq M_\star \leq M_{\star,2}$ is thus given by the following:

$$\langle N_x|M_h\rangle = \int_{M_{\star,1}}^{M_{\star,2}}\Phi_x(M_\star|M_h)\,dM_\star,$$

(B.7)

where x stands for either central or satellite. For the two components, we can then write

$$\mathcal{H}_x(k,M_h) = \frac{\langle N_x|M_h\rangle}{\bar{n}_x}\,\tilde{u}_x(k|M_h),$$

(B.8)

where $\tilde{u}_x(k|M_h)$ are the normalized Fourier transforms of the radial distribution of the central or satellite galaxies. For centrals, we assume that $\tilde{u}_x(k|M_h) = 1$ and for satellites $\tilde{u}_x(k|M_h) = \tilde{u}_h(k|M_h)$ (the satellite distribution follows the dark matter). The average number density $\bar{n}_x$ follows from

$$\bar{n}_x = \int_0^\infty \langle N_x|M_h\rangle\,n(M_h)\,dM_h,$$

(B.9)

where $n(M_h)$ is the halo mass function. For the dark matter we have the following:

$$\mathcal{H}_m(k,M_h) = \frac{M_h}{\bar{\rho}_m}\,\tilde{u}_h(k|M_h),$$

(B.10)

where $\bar{\rho}_m$ is the mean density of the Universe and $\tilde{u}_h(k|M_h)$ is the normalized Fourier transform of the NFW profile (Navarro et al. 1997). Using these ingredients, one can construct the following 1-halo and 2-halo power spectra (see also Equations 5 – 7 in van Uitert et al. 2016):

$$P_{xy}^{1h}(k) = \int_0^\infty \mathcal{H}_x(k,M_h)\,\mathcal{H}_y(k,M_h)\,n(M_h)\,dM_h$$

(B.11)

and

$$P_{xy}^{2h}(k) = P_{lin}(k)\int_0^\infty dM_{h,1}\,\mathcal{H}_x(k,M_{h,1})\,b_h(M_{h,1})\,n(M_{h,1})\int_0^\infty dM_{h,2}\,\mathcal{H}_y(k,M_{h,2})\,b_h(M_{h,2})\,n(M_{h,2}),$$

(B.12)

where $b_h(M_h)$ is the halo bias from Tinker et al. (2010) and $P_{lin}(k)$ is the linear matter power spectrum. The full GGL power spectrum is thus written as $P_{gm}(k) = P_{cm}^{1h}(k) + P_{sm}^{1h}(k) + P_{cm}^{2h}(k) + P_{sm}^{2h}(k)$, from which the $\Delta\Sigma_{gm}$ can be calculated using the following Fourier and Abel transforms (see also Equations 1 – 4 of van Uitert et al. 2016):

$$\xi_{gm}(r) = \frac{1}{2\pi^2}\int_0^\infty P_{gm}(k)\,\frac{\sin kr}{kr}\,k^2\,dk,$$

(B.13)

$$\Sigma_{\mathrm{gm}}(r_{\mathrm{p}}) = 2\overline{\rho}_{\mathrm{m}} \int_{r_{\mathrm{p}}}^{\infty} \xi_{\mathrm{gm}}(r) \frac{r\,\mathrm{d}r}{\sqrt{r^2 - r_{\mathrm{p}}^2}}\,, \tag{B.14}$$

where r_{p} is the projected separation. We also define $\overline{\Sigma}_{\mathrm{xy}}(< r_{\mathrm{p}})$ as its average inside r_{p}:

$$\overline{\Sigma}_{\mathrm{gm}}(< r_{\mathrm{p}}) = \frac{2}{r_{\mathrm{p}}^2} \int_{0}^{r_{\mathrm{p}}} \Sigma_{\mathrm{gm}}(R')R'\,\mathrm{d}R'\,, \tag{B.15}$$

which we used to define the excess surface density (ESD)

$$\Delta\Sigma_{\mathrm{gm}}(r_{\mathrm{p}}) = \overline{\Sigma}_{\mathrm{gm}}(< r_{\mathrm{p}}) - \Sigma_{\mathrm{gm}}(r_{\mathrm{p}})\,. \tag{B.16}$$

For completeness, we included the contribution of the stellar mass of galaxies to the lensing signal as a point mass, so that $\Delta\Sigma_{\mathrm{gm}}^{\mathrm{pm}}(r_{\mathrm{p}}) = M_{\star,\mathrm{med}}/\pi r_{\mathrm{p}}^2$.

Appendix C: Details of released data

Here we provide a description of the columns for the KiDS-1000 bright galaxy sample data release available at http://kids.strw.leidenuniv.nl/DR4/brightsample.php. It is separated into the photometric redshift catalog and the LePHARE derivations. The catalogs can be cross-matched by ID between each other and with the KiDS Data Release 4 main dataset available from http://kids.strw.leidenuniv.nl/DR4/index.php.

We provide a list of columns contained in the photometric redshift catalog below:

- `ID`: source identifier from the KiDS DR4 catalog.
- `RAJ2000`: right ascension (J2000).
- `DECJ2000`: declination (J2000).
- `MAG_AUTO_calib`: zero-point calibrated and extinction-corrected Kron-like elliptical aperture magnitude in the r band; `MAG_AUTO_calib` = `MAG_AUTO` + `DMAG` − `EXTINCTION_R`.
- `MAGERR_AUTO`: RMS error for MAG_AUTO.
- `zphot_ANNz2`: photometric redshift derived with ANNz2.
- `MASK`: 9-band mask information.
- `masked`: binary flag, set to 0 for unmasked and to 1 for masked objects. Use `masked == 0` for the default selection.

We also provide a list of columns contained in the stellar mass catalog below:

- `ID`: source identifier from the KiDS DR4 catalog.
- `RAJ2000`: right ascension (J2000).
- `DECJ2000`: declination (J2000).
- `K_COR_x`: the K-correction for the x-band.
- `MAG_ABS_x`: the absolute magnitude in the x-band.
- `MABS_FILTx`: the filter that is used for reference when computing the MABS.
- `CONTEXT`: a bit flag that shows which photometric bands were used in the fitting process. That is to say, if 9-band information was employed, the bit flag is as follows: 111111111=1+2+4+8+16+32+64+128+256=511. If a Z-band is missing, then the bit flag is as follows: 111101111=1+2+4+8+0+32+64+128+256=495.
- `REDSHIFT`: the redshift values used for the stellar mass computation, in this case photo-zs derived with ANNz2.
- `MASS_MED`: the median of the galaxy template stellar mass PDF measured by LePHARE. It is important to note the galaxies with MASS_MED == -99 were best-fit by a non-galaxy template, but the MASS_BEST value still shows the best fitting galaxy template mass for them, nonetheless.
- `MASS_INF`: the lower-limit on the stellar mass from the galaxy mass PDF (68% confidence level).
- `MASS_SUP`: the upper-limit on the stellar mass from the galaxy mass PDF (68% confidence level).
- `MASS_BEST`: the best-fit stellar mass estimated by LePHARE. This column should be used as the stellar mass, but it is necessary to make sure to apply the fluxscale correction (see below).
- `SFR_INF`: the lower-limit on the star formation rate from the galaxy SFR PDF (68% confidence level).
- `SFR_SUP`: the lower-limit on the star formation rate from the galaxy SFR PDF (68% confidence level).
- `SFR_BEST`: best-fit star formation rate (SFR) estimated by LePHARE.

Note 1. All the "MASS" quantities stand for $\log 10(M_{\star}/M_{\odot})$.

Note 2. Fluxscale correction: Because the GAaP photometry only measures the galaxy magnitude within a specific aperture size, the stellar mass should be corrected using a "fluxscale" parameter, which is the ratio of `AUTO` and GAaP fluxes:

$$\log 10(\texttt{fluxscale}) = (\texttt{MAG\_GAAP\_r} - \texttt{MAG\_AUTO})/2.5. \tag{C.1}$$

The "total" stellar mass in then

$$\texttt{M\_TOT} = \texttt{M\_BEST} + \log 10(\texttt{fluxscale}). \tag{C.2}$$

Similarly, also absolute magnitudes need corrections if total measurements are required:

$$\texttt{MAG\_ABS\_X}, \texttt{total} = \texttt{MAG\_ABS\_X} - 2.5 \log 10(\texttt{fluxscale}). \tag{C.3}$$

All the LePHARE quantities were computed assuming $h = 0.7$, and the estimated stellar masses are assumed to have a dependence on h dominated by the h^{-2} scaling of luminosities. Therefore, if another Hubble constant value is used, the logarithmic stellar mass in Eq. (C.2) needs to be corrected by $-2\log 10(h/0.7)$, while the absolute magnitudes in Eq. (C.3) need to have $5\log 10(h/0.7)$ added.